A Modernized View of Coherence Pathways Applied to Magnetic Resonance Experiments in Unstable, Inhomogeneous Fields

Alec A. Beaton,[1] Alexandria Guinness,[1] and John M. Franck[1]

[1] *Department of Chemistry, Syracuse University, Syracuse, NY 13210, USA*[*]

(Dated: Friday 24th June, 2022)

Over recent decades, the value of conducting experiments at lower frequencies and in inhomogeneous and/or time-variable fields has grown. For example, an interest in the nanoscale heterogeneities of hydration dynamics demands increasingly sophisticated and automated measurements deploying Overhauser Dynamic Nuclear Polarization (ODNP) at low field. The development of these methods poses various challenges that drove us to develop a standardized alternative to the traditional schema for acquiring and analyzing coherence pathway information employed by the overwhelming majority of contemporary Nuclear Magnetic Resonance (NMR) research. Specifically, on well-tested, stable NMR systems running well-tested pulse sequences in highly optimized, homogeneous magnetic fields, traditional hardware and software quickly isolate a meaningful subset of data by averaging and discarding between 3/4 and 127/128 of the digitized data. In contrast, spurred by recent advances in the capabilities of open-source libraries, the domain colored coherence transfer (DCCT) schema implemented here builds on the long-extant concept of Fourier transformation along the pulse phase cycle dimension to enable data visualization that more fully reflects the rich physics underlying these NMR experiments. In addition to discussing the outline and implementation of the general DCCT schema and associated plotting methods, this manuscript presents a collection of algorithms that provide robust phasing, avoidance of baseline distortion, and the ability to realize relatively weak signals amidst background noise through signal-averaged correlation alignment. The methods for visualizing the raw data, together with the processing routines whose development they guide should apply directly to or extend easily to other techniques facing similar challenges.

I. Introduction

This manuscript focuses on a comprehensive, non-standard approach to processing and presenting data from the various coherence pathways accessed by a Magetic Resonance (MR) experiment. This formalized approach–*i.e.*, "schema"–significantly improves the speed with which spectroscopists can develop new types of experiments. When confronted with adverse experimental circumstances, it also guides the identification of data and the development of routines that improve the quality of that data. As the authors' lab has developed an Overhauser Dynamic Nuclear Polarization (ODNP) system, these methods serve here to improve the quality of ODNP data, with particular focus on mitigating the effects of inhomogeneity and time instability of the fields offered by conventional room temperature electromagnets.

Despite the rapid, sub-nanosecond exchange of hydration water with bulk water, ODNP has the capability to measure the variation in the dynamics of hydration water molecules at specific sites, selected with nanometer-scale specificity [1, 2], as well as the accessibility of those sites to water [3, 4]. The spectroscopist can choose sites based on the location of a small molecule within a heterogeneous mixture, by linking labels to the surface of a macromolecule, or by linking them within the core of a macromolecule (or macromolecular assembly) [5, 6]. Previous literature has advocated ODNP as a tool for analyzing the hydration layer for more than 12 years [7, 8]. Furthermore, the technique employs relatively low magnetic fields (typically 0.35 T), permitting dissemination in concert with cw Electron Spin Resonance (ESR) spectroscopy [1, 2] and extension to permanent magnet systems [7, 9, 10], making it an eminently customizable technique. Nonetheless, ODNP has not yet been widely adopted for studying the hydration layer, which we ascribe in part to the practical barriers imposed by the differences between ODNP and more traditional Nuclear Magnetic Resonance (NMR) methods.

ODNP studies conducted at higher resonance frequencies [11, 12] tend to sample intramolecular motions of the spin label [13], or even correlated motions [14] that obfuscate the translational dynamics that many studies seek to recover [15]. Thus, the study of dynamics via ODNP demands relatively low fields that provide low resonance frequencies tuned to the translational dynamics of solvent molecules. Lower fields, of course, give rise to challenges with respect to spin polarization and signal amplitude in reference experiments. The integration of the NMR spectrometer with the ESR spectrometer and high power microwave amplifier required for ODNP also gives rise to a host of practical challenges. Furthermore, a full analysis of the dynamics available from ODNP involves collection of both a series of measurements of spin polarization at different levels of microwave (ESR) saturation (progressive enhancement), as well as several inversion recovery experiments acquired under different conditions to account for the slight heating, and subsequent change in relaxation rates, introduced by microwave irradiation. Careful manual analysis of the resulting data generally demands a level of fastidiousness that is unreasonable

[*] jmfranck@syr.edu

given the quantity of data under consideration.

For particular sample configurations, one can achieve reasonable ODNP results with mostly commercial hardware [2, 15–18]. Many ODNP studies follow a strategy that employs standard approaches to phase cycling and where 90°-pulse free induction decay (FID) experiments or, occasionally, standard CPMG (echo train) experiments quantify the signal intensity. Recent studies have demonstrated spectral resolution without the need for added shim coils [10], as well as examples that implement a practicable shim stack [19]. Importantly, thus far, all such advances detail engineering of the spectrometer device itself, rather than offering strategies for finer control of data visualization and processing, which could apply to all instruments. This manuscript addresses the latter concern.

Overall, the development of ODNP spectroscopy and other emerging MR techniques mandates a new approach to conventional NMR. In order to attend to all the previously mentioned problems, this manuscript carefully draws fundamental concepts of coherence transfer from the original literature [20–25], and motivation from more recent efforts [26–28], to formalize a schema in which standard code can most effectively and quickly acquire, organize, and present signal for a wide range of contexts. In particular, this schema offers a means for maximizing the information available from phase-cycled MR experiments, while still presenting (plotting) and organizing (deploying object-oriented data structures) the data in a convenient fashion. The approach to a formalized procedure for cycling the phases of pulses goes back decades [20–25], when coherence transfer (CT) maps (also known as CT pathway diagrams) were introduced as a means to understand the multiple CT pathways existing in a phase cycled pulse sequence. However, traditional experiments have been primarily concerned with how to select the desired CT pathway of interest quickly and efficiently while discarding all other information. As previously noted [26–28], this choice was originally motivated by now-antiquated hardware. Contributions toward utilizing the theory of quantum coherence transfer [29] and phase cycling [25] have been revisited in the past two decades on various occasions [26–28, 30, 31], and the recommendation of forgoing cycling of the receiver phase and separately storing each acquired transient has repeatedly arisen. Such methods rely on post-acquisition processing to select the CT pathway of interest. This work builds on these contributions by also highlighting the value in assessing "undesired" CT pathways by inspecting the other "routes" the signal follows throughout a phase cycled experiment.

In this contribution, the abbreviation domain colored coherence transfer (DCCT) refers to two key elements of the strategy: domain coloring for plotting the complex-valued data, and the formalization of CT dimensions. While the "DCCT map" refers to the colored map of the signal flowing through all coherence pathways, the "DCCT schema" refers to the overall strategy: not only plotting of the signal map, but also data organization and coding. The DCCT schema is posed as an alternative to the more traditional schema that moves quickly toward discarding all but one coherence pathway.

While the DCCT schema may be expected to aid in diagnosing instrumental shortcomings, in the applications outlined here, it has also proven useful for elucidating signal in systems and experiments that previously precluded standard ODNP analysis, thus widening the expanse of applications for ODNP. More broadly, the DCCT schema should benefit not only ODNP, but other MR methods and, more generally, other forms of spectroscopy capable of accessing multiple different coherence pathways [32–35].

The paper is organized as follows: Sec. II covers the theoretical basis of this paper, including some review, with emphasis on the mathematical basis of phase cycling (Sec. II.1.A). Sec. II.1 introduces the approach to data processing and rationalizes echo detection as yielding the benefits of the EXORCYCLE [23], while permitting routine baseline-free spectral acquisition with accurate integrals (Sec. II.1.B) and phase corrections (Sec. II.1.C and II.1.D). Next, Sec. II.1 presents the mathematics underlying a "signal averaged" alignment routine (Sec. II.1.F), the specific apodization techniques (Sec. II.1.E), and concludes with a review of ODNP theory (Sec. II.2). Since compact scripting comprises part of the results presented here, equations are referenced against an appendix (appendix A) that offers a glimpse at the corresponding code. Sec. III contains all relevant experimental details, such as sample preparation (Sec. III.1). It supplies details regarding the modular low field equipment (Sec. III.2), including a variation that relies only on a few hardware components of relatively low sophistication (Sec. III.2.C). It briefly discusses the custom Python software which serves as a cornerstone of this work (Sec. III.4). As novel data visualization/plotting techniques form a central component of the new approach, the results section (Sec. IV) begins with a demonstration (Sec. IV.1 and IV.2), along with subsequent demonstrations of specific NMR experiments presented in Sec. IV.3. This plotting technique proves particularly useful for experiments that rely on unsophisticated hardware, such as a "bare-bones" spectrometer made from non-specialized equipment (Sec. IV.3.A) and a modular system relying on a SpinCore PCI board transceiver (Sec. IV.3.B); time-variable magnetic fields present in many low-field and portable instruments also provide an opportunity to showcase the applicability of this visualization technique (Sec. IV.3.C). However, it can also (Sec. IV.3.D) demonstrate the cooperative effect of several pulses and can be deployed on standard commercial instrumentation. The DCCT schema for organizing and plotting the data then motivates and facilitates the algorithms in Sec. IV.4, which presents phasing (Sec. IV.4.A), correlation-based frequency alignment in the presence of phase cycling at low signal to noise ratio (SNR) (Sec. IV.4.B), and apodization (Sec. IV.4.E). Collec-

tively, these processing procedures prove extremely flexible and adaptable to the inversion recovery (Sec. IV.4.C) and to the progressive enhancement (Sec. IV.4.D) experiments that are essential to recording data relevant to hydration dynamics. The schema proves particularly useful in a uniquely low SNR case scenario (Sec. IV.4.G), which highlights the utility of this means of data handling and presentation. Sec. V and VI place the schema in the broader context of existing NMR literature and forecast future applications. In particular, these techniques enable synergy between data acquisition and processing, which relies less on starting infrastructure and allows for greater sophistication in the processed results. Looking forward, the DCCT map and the resulting signal optimization techniques facilitate not only improvements in processing methodologies such as those presented here but also provide the framework for many future advances.

II. Theory

II.1. Data Processing

Several sections below utilize the notation

$$c(\Delta x) = f(x) \star g(x)$$

for the correlation function, such that:

$$c(\Delta x) = \int_{-\infty}^{\infty} f^*(x) g(x + \Delta x) dx \tag{1}$$

Aside from providing compactness, this notation emphasizes the fact that a Fourier domain multiplication ($\tilde{c}(\nu) = \tilde{f}^*(\nu)\tilde{g}(\nu)$) significantly outperforms the numerical integration of Eq. (1).

II.1.A. Phase Cycling

Throughout, the software utilizes the standard relationship that [25]:

$$s(\Delta p, t) = \frac{1}{\sqrt{n_\varphi}} \sum_{j=0}^{n_\varphi - 1} e^{-i2\pi \Delta p_j \varphi_j} s(\varphi_j, t) \tag{2}$$

where n_φ gives the number of phase cycle steps and, following standard notation, Δp_j indicates the coherence change during pulse j. The phase angle φ_j has units of [cyc] = [rad]/2π, such that an x pulse has $\varphi = 0$ cyc a y pulse has $\varphi = 0.25$ cyc, *etc.*; the resulting Δp_1 are then unitless. This manuscript employs the phrasing that Eq. (2) relates the "phase cycling domain" (φ_j) to the Fourier conjugate "coherence transfer domain" (Δp_j).

When the pulse sequence cycles the phase of multiple pulses, the signal in the coherence transfer domain, $s(\Delta p_1, \Delta p_2, \cdots, \Delta p_N, t)$, derived from an N-dimensional Fourier transform of the phase cycling domain signal, gives the component of the signal that changes by Δp_1 during the first pulse, Δp_2 during the second pulse, *etc.* Thus, $s(\Delta p_1, \Delta p_2, \cdots, \Delta p_N, t)$ includes the signal for all distinguishable coherence transfer pathways. The Δp dimensions are subject to standard Fourier aliasing, resulting from the Nyquist theorem. When a single coherence transfer pathway is selected, this aliasing collapses to the well-known rules laid out in the seminal phase cycling contribution from Bodenhausen, Kogler, and Ernst [25, 36].

II.1.B. Deriving Integrals from Echoes

ODNP relies on high-quality quantitative NMR that requires properly phased signal without a baseline. The inhomogeneous fields and low SNR conditions commonly encountered in ODNP pose some obstacles toward routinely acquiring data with correct phasing that avoids baseline artefacts. Fortunately, the echo-based signal acquisition advocated in this work not only refocuses inhomogeneities but also circumvents baseline problems by recovering signal typically lost to the pulse deadtime, thus yielding distortion-free early time points of the FID [37]. Echo-based signal acquisition also reaps the benefits provided by the EXORCYCLE [23] and permits straightforward automated approaches for signal phase correction. Typical 90° pulse and subsequent 180° pulse lengths are advantageously short (≤ 10 µs) in most ODNP systems, while T_2 times are long (hundreds of ms to s), garnering these benefits virtually free of cost.

Phase correction routines identify the origin of the time axis ($t = 0$), defined as the time point at which all the isochromats in the signal present the same phase [37, 38]. For an idealized (noise-free) echo, $t = 0$ corresponds to the peak of the echo. Echoes symmetric about $t = 0$ yield purely real Fourier transforms, but echoes generated in response to short echo times (which refocus shortly after the 180° pulse) can also be converted to FID's *via* multiplication by an appropriate Heaviside function, $h(t)$:

$$s_{FID}(t) = s(t)h(t) = \begin{cases} 0 & t < 0 \\ \frac{1}{2}s(t) & t = 0 \\ s(t) & t > 0. \end{cases} \tag{3}$$

Before the code implements Eq. (3) it must adjust the origin of the time axis, possibly by a non-integral multiple of the dwell time (the time-domain sampling interval). The pySpecData Python library (developed in-house and used here throughout) facilitates these manipulations by maintaining the time coordinates of the signal and providing a compact notation that selects and manipulates the signal based on its time coordinates (listing A.1). Upon Fourier transformation, the pySpecData library automatically generates an appropriate axis of frequency coordinates and, for time axes that do not begin at $t = 0$, automatically multiplies in the frequency domain by the appropriate first-order phase shift.

The relatively simple treatment of short-time echoes contrasts with the behavior of FIDs arising in response to an isolated 90° pulse. Assuming the frequency-domain signal comprises a superposition of Lorentzians, beginning acquisition on a time axis (t') at some time point t_d after the nominal center of the echo (*s.t.* $t = t' + t_d$)

results in

$$\sum_j e^{i2\pi\nu_j t - R_j t} h\left(t - t_d\right) = \sum_j e^{i2\pi\nu_j t_d} e^{-R_j t_d} e^{i2\pi\nu_j t' - Rt'} h(t') \tag{4}$$

– *i.e.*, each resonance changes slightly in amplitude and phase. Of course, in mild cases, a uniform first-order phase shift can correct for the change in phases. However, it is also known that issues arise from either distortion of the initial FID datapoints [37] as well as from the interference of nearby peaks (especially their dispersive components). These issues are particularly noticeable when choosing a value of t_d that is a non-integer multiple of the dwell time [39, 40]. While Linear Prediction (LP) and other techniques can mitigate these effects in post-processing, echoes offer an alternative solution to signal detection where no part of the time domain must be interpolated or predicted.

II.1.C. Zeroth-Order Phase Correction

Very simple methods for calculating zeroth-order (frequency-independent) phase correction behave well when all peaks are positive; however, both for inversion recovery and for ODNP enhancement curves, the sign of any given peak is unknown. Therefore, given a collection of complex datapoints (s_k) assumed to be distributed primarily along the real axis of the complex plane and then rotated by some arbitrary constant (zeroth-order) phase, the principle axis of the matrix

$$\begin{aligned} I_{ij} &= \sum_{k=1}^{N} \begin{bmatrix} |s_k|^2 - \Re\left[s_k\right]^2 & -\Re\left[s_k\right]\Im\left[s_k\right] \\ -\Re\left[s_k\right]\Im\left[s_k\right] & |s_k|^2 - \Im\left[s_k\right]^2 \end{bmatrix} \\ &= \sum_{k=1}^{N} \begin{bmatrix} \Im\left[s_k\right]^2 & -\Re\left[s_k\right]\Im\left[s_k\right] \\ -\Re\left[s_k\right]\Im\left[s_k\right] & \Re\left[s_k\right]^2 \end{bmatrix} \end{aligned} \tag{5}$$

(motivated by the formula for the inertia tensor) would provide the vector in the complex plane that the real axis had been rotated to. The zeroth order phase correction that corresponds to rotating this axis to align with the real axis performs well even when the datapoints have a variable sign.

II.1.D. First-Order Phase Correction

The expression:

$$\tau_{echo} \approx \tau + 2t_{90}/\pi \tag{6}$$

provides a reasonable approximation to the actual observed τ_{echo} based on the ninety time t_{90} and inter-pulse delay τ in a spin echo experiment [37, 41]. But, in practice, the existence of hardware trigger delays, group delays due to line transmission, *etc.*, means that the exact position of the echo center must be determined experimentally.

If the timescale of the inhomogeneous decay (T_2^*) exceeds the required timing correction, the determination of the center maximum of the echo frequently proves less trivial than expected. In particular, the presence of noise complicates attempts to choose between the amplitude of time points near the peak of the echo, where the magnitude is relatively flat as a function of time. Furthermore, echoes resulting from experiments that invert some isochromats but not others (or from antiphase signal) will not necessarily present maximum amplitude at the center of the echo.

Two strategies yield more robust procedures for finding the echo center:

The first strategy exploits the fact that the echo signal in the time domain must have Hermitian symmetry ($s(t) = s^*(-t)$). Therefore, the cross-correlation of the echo waveform with its Hermitian conjugate can identify the timing discrepancy between the instrumentally assigned time axis and the "true" time axis, where $t = 0$ corresponds to the echo center.

Invoking established procedure for analogous calculations in the molecular dynamics literature [42], this strategy begins by zero-filling the signal, $s(t)$, to twice its length. For a discrete signal with N datapoints, the resulting zero-filled signal $s_{zf}(t)$, has length $2Nt_{dw}$, where t_{dw} (the dwell time) gives the separation between datapoints in the time domain. The following equations will utilize the fact that s_{zf} (or any signal treated by a discrete Fourier Transform) is mathematically modeled as infinitely repeating, with a periodicity equal to its length ($2Nt_{dw}$). For any real inhomogeneous broadening, the cost function

$$c(\Delta t) = \frac{t_{dw}}{\Delta t + t_{dw}} \int_{-\Delta t}^{0} \left| e^{i\varphi_0} s_{zf}^*(-t) - e^{-i\varphi_0} s_{zf}(t + \Delta t) \right|^2 dt \tag{7}$$

should drop to a minimum for a value of Δt, named Δt_{min}, that gives the time shift needed to align the echo center in $s_{zf}(t)$ with the echo center in the Hermitian conjugate $s_{zf}^*(-t)$ (bearing in mind the periodicity of both functions). Therefore $\Delta t_{min}/2$ corresponds to the difference between the original (instrumental) $t = 0$ and the center of the echo. In Eq. (7), the integral limits run only over times where the integrand is non-zero and multiplication with the term outside the integral normalizes by the number of integrated datapoints; φ_0 signifies that the zeroth-order phasing of the signal remains unknown until the determination of the echo center. Expansion of the modulus squared yields

$$c(\Delta t) = \frac{t_{dw}}{\Delta t + t_{dw}} \left[\int_{-\Delta t}^{0} \left| s_{zf}^*(-t) \right|^2 + \left| s_{zf}(t + \Delta t) \right|^2 dt - 2 \int_0^{2Nt_{dw}} \Re\left[e^{-i2\varphi_0} s_{zf}(t + \Delta t) s_{zf}(-t) \right] dt \right], \tag{8}$$

where the limits of the third term have been expanded into regions where the integrand is zero. Substitution of integration variables and utilization of the definition of the correlation symbol then yields

$$c(\Delta t) = \frac{2t_{dw}}{\Delta t + t_{dw}}\left[\int_0^{\Delta t} |s_{zf}(t)|^2\, dt - \Re\left[e^{-i2\varphi_0} s^*_{zf}(-t) \star s_{zf}(t)\right]\right] \tag{9}$$

Finally, note that the choice of φ_0 that will minimize the previous expression is simply the phase of $s_{zf}(t)$ at the echo center. Therefore, the expression

$$c'(\Delta t) = \frac{2t_{dw}}{\Delta t + t_{dw}}\left[\int_0^{\Delta t} |s_{zf}(t)|^2\, dt - \left|s^*_{zf}(-t) \star s_{zf}(t)\right|\right] \tag{10}$$

has a minimum at the same Δt as Eq. (9). As the Fourier transform of the second term in Eq. (10) is the square of the Fourier transform of $s_{zf}(t)$, the Hermitian conjugate shown in the second term is never explicitly calculated.

The second phasing strategy relies on the fact that the integral of the absolute value of the absorptive component of a Lorentzian peak is smaller than the absolute value of the dispersive component. Previous literature has extensively employed this principle for first order phase correction of FIDs [43]. In the present context, this amounts to finding the minimum of the cost function

$$C(t_d) = \int \left|\Re\left[e^{-i\varphi_0} h(t - t_d) s(t)\right]\right| dt. \tag{11}$$

Of course, this cost will artificially fall off as t_d is pushed to later portions of the signal decay, so we instead optimize:

$$C(t_d) = \frac{\int \left|\Re\left[e^{-i\varphi_0} h(t - t_d) s(t)\right]\right| dt}{\int \left|\Im\left[e^{-i\varphi_0} h(t - t_d) s(t)\right]\right| dt}. \tag{12}$$

While this cost function might be expected to fluctuate significantly at low signal energies, it can still provide useful context, especially for sequences that employ standard 90° pulses or very short echo times.

II.1.E. Linewidth and Apodization

For various purposes, the spectroscopist may desire to determine a generic measure of linewidth, defined even for complicated lineshapes. For low-field data, standard apodization techniques (such as Lorentzian-to-Gaussian transformations) prove useful on several fronts. Therefore, a consistent definition of standard lineshapes and quantification of their signal energy ($\propto \int |s(t)|^2 dt = \int |s(\nu)|^2\, d\nu$) are advantageous.

The Fourier transform (with limits $\pm\infty$) of

$$s_G(t, \lambda_G) = \exp\left(-\frac{\pi^2 \lambda_G^2 t^2}{4 \ln 2}\right) \tag{13}$$

is a Gaussian with full-width-half-maximum (FWHM) of λ_G, integral 1, and signal energy

$$E_G(\lambda_G) = \sqrt{\frac{2 \ln 2}{\pi}} \frac{1}{\lambda_G}, \tag{14}$$

while the Fourier transform of

$$s_L(t, \lambda_L) = \exp\left(-\pi \lambda_L |t|\right) \tag{15}$$

is a Lorentzian with FWHM of λ_L, integral 1, and signal energy

$$E_L(\lambda_L) = \frac{1}{\pi \lambda_L}. \tag{16}$$

The preceding statements are true for spin echo signal that includes both a rising refocusing period as well as a decay. Signal comprising exclusively a perfect FID (Eq. (3)) would yield an integral with half the size and an energy of half the magnitude.

Apodization requires some knowledge of the original experimental linewidth for optimal results. However, the presence of inhomogeneities can complicate the definition of such a linewidth. A fairly robust strategy for determining the generalized linewidth can be adopted from a strategy of fitting the envelope (the sum of the absolute value of the time domain waveform along any indirect dimensions) of the time domain waveform to either a Gaussian or decaying exponential function. The folded normal distribution [44] gives the functional form of the time domain signal envelope as $y'(t)$:

$$y'(t) = \sigma_n \sqrt{\frac{2}{\pi}} \exp\left(-\frac{A^2 y(t)^2}{2\sigma_n^2}\right) + A y(t) \mathrm{erf}\left(\frac{A y(t)}{\sqrt{2\sigma_n^2}}\right) \tag{17}$$

where $y(t)$ is either Eq. (13) or Eq. (15), σ_n is the standard deviation of the instrumental noise, and A is the signal amplitude.

Finally, when considering the Lorentzian-to-Gaussian transformation, a range of final linewidths could be chosen, with narrower linewidths reducing the SNR. This manuscript will consider two cases. First, when SNR considerations are significant, it is sensible to choose the λ_G of the resulting (output) Gaussian to be of equal integral and energy to the Lorentzian of intrinsic linewidth λ_L. Specifically, this corresponds to $\lambda_G = \lambda_L \sqrt{2\pi \ln 2}$, for which $E_G(\lambda_G) = E_L(\lambda_L)$, and, overall, an apodization operation of:

$$s'(t) = s(t) \exp\left(\left(-\frac{\pi^2 \lambda_L t^2}{2} + |t|\right) \pi \lambda_L\right) \tag{18}$$

where λ_L comes from the generic linewidth determined from the signal envelope. In the second case,

$$s'(t) = s(t) \exp\left(\left(-\frac{\pi \lambda_L t^2}{4 \ln(2)} + |t|\right) \pi \lambda_L\right) \tag{19}$$

implements an equal linewidth transformation, replacing a Lorentzian of λ_L with a Gaussian of the same FWHM.

II.1.F. Alignment by Cross-Correlation

Field fluctuations of permanent magnets and room-temperature electromagnets lead to slight shifts in the resonance frequencies of subsequent transients. Some previous methods for spectral alignment have relied on iterative Bayesian [45] or other statistical means to align signal [46] while others invoke correlation of spectral fragments [47, 48]. These methods typically operate on the absolute value of the signal or well-phased signal, have not been implemented for low-field signal, or do not allow for independent shifting of phase cycled transients. More recent studies have demonstrated the promise of cross-correlation of transients as a simple and potent technique to align NMR transients in the presence of a variable field in low-field systems [19]. In fact, cross-correlation can explicitly deal with complex signals undergoing phase cycling and can be clearly mathematically justified. Motivated by this, we introduce a specific variant of cross-correlation (signal-averaged mean-field cross-correlation) that can function even under circumstances where individual pairs of transients do not offer sufficient SNR for alignment.

Consider inspecting the signal from two transients in the frequency domain, $S_j(\nu)$ and $S_m(\nu)$, shifting S_j to the left by $\Delta\nu_j$ to maximize the norm of the resulting signal $|S_m(\nu) + S_j(\nu + \Delta\nu_j)|^2$ – *i.e.*, consider maximizing the expression:

$$\begin{aligned}\int |S_m(\nu) + S_j(\nu + \Delta\nu_j)|^2 \, d\nu \\ = \int |S_m(\nu)|^2 \, d\nu \\ + \int |S_j(\nu + \Delta\nu_j)|^2 \, d\nu \\ + 2\int \Re\left[S_m^*(\nu) S_j(\nu + \Delta\nu)\right] d\nu\end{aligned} \tag{20}$$

S_j and S_k are periodic (because Fourier transformation of discretely sampled time domain signals generates periodic frequency domain signals). Therefore, not only the first term in Eq. (20), but also the second term, remains constant for all values of $\Delta\nu_j$. Consequently, the problem of aligning the signals in the frequency domain to give maximum overlap mathematically corresponds *exactly* to the much simpler problem of finding the maximum of the real part of the correlation function ($C(\nu_j)$) in the third term, where

$$\begin{aligned}C(\Delta\nu_j) = \int S_m^*(\nu) S_j(\nu + \Delta\nu_j) d\nu \\ = S_m(\nu) \star S_j(\nu)\end{aligned} \tag{21}$$

and where the second equality makes use of the $\star$ symbol (Eq. (1)), and the FFT makes calculation trivial and fast. Difficulties in applying this mathematical truism to real data appear when considering noise and phase cycling.

As implicitly recognized in previous literature [48], note that Eq. (21) integrates over regions of ν that potentially contain exclusively noise. Noisy transients will lead to noisy correlation functions, meaning the position of the maximum of Eq. (20) will be influenced by the maximum of the signal and the presence of noise. This effect will degrade SNR of the correlation function even for values of $\Delta\nu$ that correspond to well-aligned signal, making it important to leave out frequencies that contain only noise.

Even then, a single transient may not provide sufficient SNR to even identify the presence or absence of signal. Importantly, the generalization of Eq. (21) to the case of more than two transients involves the consideration of not only the overlap of adjacent transients, but the total overlap of all transients, and requires finding the maximum of the real part of:

$$\begin{aligned}C(\Delta\nu_1, \cdots, \Delta\nu_J) = \sum_{\substack{m,j \\ m\neq j}} \int S_m^*(\nu + \Delta\nu_m) \\ \times S_j(\nu + \Delta\nu_j) d\nu \\ = \sum_{\substack{m,j \\ m\neq j}} S_m(\nu + \Delta\nu_m) \star S_j(\nu)\end{aligned} \tag{22}$$

to determine the corrective shifts in an experiment with J transients. Note that Eq. (22) depends on the shifts for all transients, simultaneously; thus, the ellipsis indicates the presence of J arguments to the highly multi-dimensional function C, while the sum varies m and j across all possible combinations of the J transients. The approach to optimizing C adopted here involves finding a "mean field"-type solution that fixes all but one of the $\Delta\nu_j$

$$C_{m.f.}(\Delta\nu_j) = \sum_{\substack{m \\ m\neq j}} \Re\Big[S_m(\nu) \star S_j(\nu)\Big], \tag{23}$$

where the correlation resulting from $\star$ is a function of $\Delta\nu_j$ (Eq. (1)), with the position of all other transients ($\Delta\nu_m$ in Eq. (22)) held constant. This expression generates a single one dimensional curve for each transient (of subscript j), each of which yields a clear optimal $\Delta\nu_j$. This solution requires iterating until the list of $\Delta\nu_j \rightarrow \Delta\nu_m$ values remains consistent from one iteration to the next: typically 3-10 iterations. While requiring a more laborious computation by demanding calculation of all possible correlation functions between all possible transients (rather than merely, *e.g.*, adjacent transients in a time series), the sum in this expression actually involves a signal averaging of the correlation function and proves particularly important in the case where individual transients

may have particularly low SNR. We, therefore, refer to Eq. (23) and its generalization to phase-cycled signal, below, as a "signal-averaged correlation function."

Aligning in the presence of a phase cycle comprises the second main consideration here. Following the DCCT schema, one can treat phase cycling as an added dimension, then Fourier transform into the coherence domain, and then seek to optimize the portion of the (Frobenius) norm of the signal that varies with the frequency shift. The norm squared is:

$$C(\Delta\nu_{1,1},\cdots,\Delta\nu_{J,K}) = \sum_l \int \Big| \sum_{j,k} e^{-i2\pi\varphi_k\Delta p_l} s_{j,k}(\nu+\Delta\nu_{j,k},\varphi_k)\Big|^2 d\nu \tag{24}$$

for an experiment with J repeated scans cycled over K phases. Here, the sum over j spans all signal averaged repeated scans, while the sum over k spans all pulse phases and the sum over l spans all coherence transfer values. Again (as indicated by the ellipsis) C is highly multidimensional. As in the 1D case, one could consider optimizing C by iteratively optimizing the individual mean field correlation functions arising from the cross-terms (between j, k *vs.* m, n terms) of Eq. (24) and iterating $\Delta\nu_{j,k} \rightarrow \Delta\nu_{m,n}$ to convergence. Isolating the cross terms, analogously to Eq. (20) $\rightarrow$ Eq. (21), and rearranging slightly yields:

$$C_{m.f.}(\Delta\nu_{j,k};\Delta p_l) = \Re\Bigg\{ e^{-i2\pi\varphi_k\Delta p_l} \sum_n e^{+i2\pi\varphi_n\Delta p_l} \times \sum_{\substack{m\\ m\neq j}} \int \big[s^*_{m,n}(\nu,\varphi_n) \times s_{j,k}(\nu+\Delta\nu_{j,k},\varphi_k)\big] d\nu \Bigg\} \tag{25}$$

The cross-terms of Eq. (24) involve summing $C_{m.f.}$ over all values of Δp_l; however, as rationalized later, the code will frequently only calculate $C_{m.f.}(\Delta\nu_{j,k};\Delta p_l)$ for a subset of Δp_l values, so Eq. (25) will prove more convenient. After defining $\Delta\varphi_n = \varphi_k - \varphi_n$, rearranging the summations, and taking advantage of the $\star$ symbol (now redefined to generate a function of $\Delta\nu_{j,k}$), this becomes

$$C_{m.f.}(\Delta\nu_{j,k};\Delta p_l) = \sum_n \Re\Bigg\{ \sum_{\substack{m\\ m\neq j}} \Big[\sum_n \big[e^{-i2\pi\Delta\varphi_n\Delta p_l} s_{m,n}(\nu,\varphi_k+\Delta\varphi_n)\big] \star s_{j,k}(\nu,\varphi_k)\Big] \Bigg\} \tag{26}$$

Note that the code that implements the innermost sum first introduces a new dimension ($\Delta\varphi_n$) with the same size and coordinates as both φ_n and φ_k, and along which the elements of the signal are duplicated and then cyclically permuted (rolled) along the φ_k dimension by the index n. It then FFTs along the new $\Delta\varphi_n$ dimension. For example, if data arises from a pulse sequence repeated over eight scans, where each scan involves cycling the phase of the pulse φ_k in four steps and $C_{m.f.}$ is only calculated for a single value of Δp_l, then Eq. (26) yields a set of $8\times4 = 32$ functions $C_{m.f.}(\Delta\nu_{j,k};\Delta p_l)$ for the 32 transients that not only cross-correlate different transients repeated with the same pulse phases (subscripted by j) but also transients that differ only in the choice of pulse phase (subscripted by k). The maximum of the real part of each of the 32 functions indicates the frequency shift to be applied to the 32 transients. The Δp_n that appears in Eq. (26) represents the difference in phase between the two functions that are being correlated; the choice of Δp_l uses Δp_n to determine whether the phase term in Eq. (26) leads to addition, subtraction, or quadrature addition of the different contributions that sum to yield the correlation function.

Importantly, since the signals are periodic, Plancherel's theorem implies that different frequency shifts applied to different spectra along an indirect dimension cannot change the norm of the data. Therefore, unlike the case of frequency shifts among transients that are signal averaged (the j or m indices in Eq. (23) and Eq. (25)), differences between the frequency shifts along the phase cycling dimension (the k or n indices) cannot lead to optimization of Eq. (24).

Both the specifics of this effect and a workaround can be considered with the simplest possible example: signal acquired with two transients under a two-step phase cycle, as exemplified in Fig. 1. Specifically, consider an idealized resonance, arising from an FID, of FWHM λ_L:

$$s(\nu,\varphi) = \left(\frac{e^{i\varphi}}{\sqrt{2}}\right) \frac{\pi\lambda_L}{i2\pi(\nu-\nu_0)+\pi\lambda_L} \tag{27}$$

acquired with $\varphi = 0$ rad and $\varphi = \pi$ rad (*i.e.*, using a two-step phase cycle resulting in two separate transients). Upon discrete Fourier transformation (dimension of length 2) along φ into the conjugate domain Δp, the signal ($\Delta p = -1$, aliased to $\Delta p = +1$) appears centered about ν_0 at $\Delta p = +1$ (dashed red lines in Fig. 1a). Such a signal, with $\lambda_L = 2/\pi$ has a signal energy (norm squared) of 1, both before and after unitary Fourier transformation along the φ dimension. For this idealized signal, no signal appears in the other coherence pathway ($\Delta p = 0$; blue lines in Fig. 1a). In the case where field fluctuations shift one of the transients by $\Delta\nu \gg \lambda_L$ (Fig. 1b), one transient presents signal centered at ν_0 and another at $\nu_0 + \Delta\nu$. The signal must still have a signal energy of 1, so that after Fourier transformation from φ to Δp, when the signal energy from both peaks (ν_0 *vs.* $\nu_0+\Delta\nu$) spreads equally across $\Delta p = 0$ and $\Delta p = 1$, and breaks into 4 peaks, each has signal energy of 0.25, as shown in Fig. 1b. Notably, misalignment spreads the signal energy both along the frequency domain (ν) and the coherence

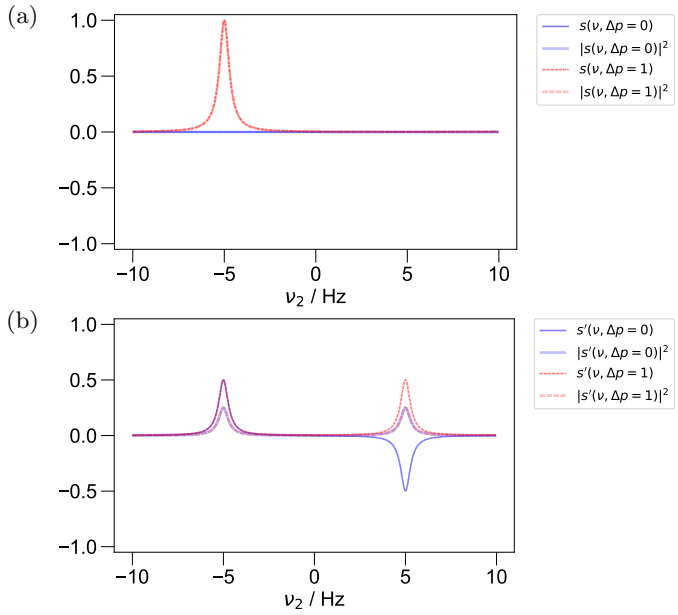

FIG. 1. A Lorentzian peak, following Eq. (27) with $\lambda_L = 2/\pi$, illustrates the simplest example of how field fluctuations (typically present in low-field data) impact phase cycled data and offers insight into a method of alignment. The resonance frequency remains fixed at -5 Hz for both steps of the phase cycle in (a), while the resonance frequency for the two steps of the phase cycle is set to -5 Hz and $+5$ Hz, respectively, in (b), simulating misaligned data. Dashed red represents the desired coherence pathway ($\Delta p = +1$) and solid blue represents the undesired pathway ($\Delta p = 0$). The bolder lines show the data's magnitude squared, and, for the choice of $\lambda_L = 2/\pi$, the energy of the peak (the area under the magnitude squared) is equal to the peak height. The lineshapes plotted here emphasize that the overall signal energy of the data remains preserved, whether the data is aligned or not, even though misalignment spreads signal intensity over a wider bandwidth in both the frequency (ν) and coherence (Δp) domains.

domain (Δp). This effect will also appear, to a less dramatic extent, in experimental data (*e.g.*, Figs. 11 and 12).

A different signal metric – specifically a "masked norm" – provides an analog of Eq. (24):

$$N'(\Delta\nu_{1,1},\cdots,\Delta\nu_{J,K}) = \sum_l \int f_{mask}(\nu,\Delta p_l)\Big|\sum_{j,k} e^{-i2\pi\varphi_k\Delta p_l} \times s_{j,k}(\nu+\Delta\nu_{j,k},\varphi_k)\Big|^2 d\nu \tag{28}$$

where the new function $f_{mask}(\nu,\Delta p_l)$ is the (real and positive) "mask" function. With an appropriate choice of the mask function, the masked norm N' will indeed only rise to a maximum for the choice of $\Delta\nu_{j,k}$ that aligns the transients.

For instance, consider a mask function that is uniform along Δp and significantly exceeds 0 along ν only in a bandwidth of similar size to the linewidth. In the example of Eq. (28), only 2 of the 4 peaks observed in Fig. 1b, each peak with an energy of 0.25, would contribute to the calculated masked norm. Thus, the masked norm for properly aligned signal (~ 1) would exhibit $\sim 2\times$ greater energy than that of the masked norm for the unaligned signal (~ 0.5). Attempting to optimize $N'(\Delta\nu_{j,k})$ for this choice of f_{mask} therefore would result in aligned signal. Considering f_{mask} of opposite construction – this time uniform along ν and only nonzero for $\Delta p_l = +1$ (the expected coherence pathway of Eq. (27)) would lead to a similar optimization. Meanwhile, a f_{mask} selective along both Δp and ν would lead to a $4\times$ greater energy of the masked norm for the aligned signal relative to the energy of the unaligned signal – *i.e.*, a 4-fold preference for aligned signal over unaligned signal.

Thus, to align signal in the presence of phase cycling, one should construct a $f_{mask}(\nu,\Delta p_l)$ that is nonzero along ν only over a bandwidth similar to that of the signal and nonzero along Δp_l only for values of Δp_l where the signal or significant artefacts appear. Then, one can iteratively optimize the masked version of the 2D mean-field correlation function shown in Eq. (26):

$$C'_{m.f.}(\Delta\nu_{j,k};\Delta p_l) = \sum_n \sum_{\substack{m\\ m\neq j}} \Re\Big\{ s_{m,n}(\nu,\varphi_k+\Delta\varphi_n) \star \sum_l \left[e^{-i2\pi\Delta\varphi_n\Delta p_l} f_{mask}(\nu,\Delta p_l) s_{j,k}(\nu,\varphi_k)\right]\Big\} \tag{29}$$

where, as before, the $\star$ operation operates along the ν domain to yield a function of $\Delta\nu_{j,k}$ (and not ν), and where $s_{j,k}$ is a function of 3 variables: ν, φ_k, and $\Delta\varphi_n$. In comparing to other alignment methods, note that while the mask can and does serve as a type of "reference spectrum" for the alignment, the signal-averaged correlation function still drives alignment of the spectra; in fact, the two operate cooperatively, with the mask helping to improve the signal to noise (*via* filtering) of the correlation function, and the signal-averaged correlation function driving alignment of the sharper features of the spectrum.

II.2. ODNP

An ODNP experiment simultaneously excites ESR with microwave (μw) radiation and detects NMR with rf. It analyzes the mobility of water and discriminates motion at the timescale of the NMR resonance (here $\sim$ 15 MHz) from motion at the timescale of the ESR resonance ($\sim$ 9.8 GHz). Two different relaxivities, k_{low} and k_σ [$\mathrm{M}^{-1}\mathrm{s}^{-1}$], sample the nuclear spin single-flips, and the cross relaxation between the unpaired electron and the nuclei, respectively [15].

Some of the experiments reported here measure the signal intensity, $I(p)$, as a function of microwave power, p, where $I(0)$ gives the thermally polarized (*i.e.*, Boltzmann, non-hyperpolarized) signal intensity. The results follow the established convention [3] of defining the trans-

ferred polarization as $\varepsilon(p) = (I(0) - I(p))/I(0)$, so that

$$\varepsilon(p) = \left(\frac{s(p)}{R_1(p)}\right) k_\sigma C_{SL} \left|\frac{\omega_e}{\omega_H}\right| \tag{30}$$

where $s(p)$ is the electron spin saturation factor (averaged across all hyperfine transitions) as a function of microwave power, $R_1(p)$ [s^{-1}] is the longitudinal relaxation rate of the ^{1}H nuclei as a function of microwave power, ω_e [rad/s] is the Larmor frequency of the electron, ω_H [rad/s] is the Larmor frequency of the ^{1}H nucleus, with, *e.g.*, $|\omega_e/\omega_H| = 659.33 \pm 0.05$ for TEMPOL in aqueous solution [2].

Importantly, minuscule variations in temperature can significantly change $R_1(p)$, thus affecting the overall $\varepsilon(p)$ [2]. For this reason, ODNP measurements of dynamics depend on efficient $R_1(p)$ measurements to enable accurate quantification of the product of the cross-relaxivity (k_σ) and the saturation factor:

$$k_\sigma s(p) = \frac{\varepsilon(p) R_1(p)}{C_{SL}} \left|\frac{\omega_H}{\omega_e}\right|. \tag{31}$$

Eq. (31) typically follows an asymptotic form, even when $\varepsilon(p)$ does not [2, 49]. $R_1(p)$ is found from inversion recovery experiments at different powers by fitting each set of data to the equation

$$M(\tau) = M_\infty(1 - (2 - e^{-WR_1})e^{-\tau R_1} \tag{32}$$

where τ represents the variable delays used in each inversion recovery experiment and W represents the magnetization recovery time [50]. Therefore, the typical procedure for ODNP entails collecting several individual NMR experiments: a series of 1D NMR spectra, recorded at different microwave powers to obtain a progressive enhancement ($E(p) = 1 - \varepsilon(p)$) curve, and also several inversion recovery experiments, recorded at different microwave powers to obtain $R_1(p)$. This contribution does not focus on the determination of k_σ for particular samples but on the acquisition of progressive enhancement and relaxation curves themselves.

III. Experimental

III.1. Sample Preparation

The spin probe TEMPOL (4-hydroxy-2,2,6,6-tetramethylpiperidin-1-oxyl, Sigma-Aldrich) provides the unpaired electron for all ODNP measurements shown here, including several studies that utilize pure solutions of the spin probe in water and in toluene (Sigma-Aldrich).

For reverse micelle measurements, CTAB (hexadecyltrimethylammonium bromide, 0.186 g, 57 mM, Sigma-Aldrich) was dissolved in 8.39 mL of CCl_4, into which hexanol co-surfactant (0.460 g, 502 mM) was added. After addition of water (68 mg, 424 mM), a total H_2O:CTAB:hexanol of 7.45:1:8.82 was obtained. The sample was then vortexed 2 × 30 s, allowed to rest for 5 min at r.t., and loaded into a 0.6 × 0.8 mm capillary tube (Fiber Optic Center, New Bedford, MA, USA) that was flame-sealed at both ends.

For measurements of water samples not requiring ODNP, a 13 mM $NiSO_4$ (Fisher) solution was prepared.

III.2. Spectrometer with Minimalistic, Modular Design

Most data was acquired on a modular NMR spectrometer operating in tandem with a Bridge12 microwave power source and the magnet of a Bruker E500 cw EPR with SuperX bridge. The modular design of the system makes several different configurations possible.

III.2.A. ODNP Configuration and Probe

The most frequently used configuration employs a home-built probe (4.8 µL sample volume, 17 mm length) that integrates specifically with the Bruker Super High Sensitivity Probehead X-Band resonator (ER 4122 SHQE). A SpinCore RadioProcessor-G transceiver (a TTL and rf waveform generator and rf digitizer), packaged as a PCI board, interfaces with the probe by way of a homebuilt passive duplexer and standard LNA receiving chain, as well as a SpinCore rf amplifier powered by generic power supply electronics.

III.2.B. Large Sample 15 MHz Probe

Some experiments that do not require high-power microwaves instead utilize a probe with a solenoid coil, rather than the typical hairpin loop employed in the ODNP experiments. The solenoid probe, enclosed in a shielding box, accommodates a sample size of 390 µL (approximate sample height of 20 mm in a 5 mm o.d. NMR tube), allowing for better signal to noise. Notably, however, the larger sample size also leads to significantly larger field inhomogeneities when placed in the same location (within the EPR magnet gap) as the ODNP probe.

III.2.C. NMR spectrometer independent of microwave electronics

A simple off-the-shelf oscilloscope and arbitrary waveform generator can function as an alternative to the SpinCore transceiver board. The GW-Instek AFG-2225 waveform generator generates the pulse waveforms that are amplified by an ENI 3100L RF amplifier (does not require de-blanking), while the GW-Instek GDS-3254 oscilloscope digitizes the signal after passing through an analog low-pass filter (MiniCircuits SLP-21.4+). The bandwidth (250 MHz) and sampling rate (5 GSPS) of the oscilloscope both exceed the bandwidth of the low-pass filter.

In practice, this configuration was used before the SpinCore for setup and diagnostic purposes.

III.3. Commercial High-Field NMR

A high-field Bruker AVANCE III HD spectrometer, equipped with a broadband room temperature SMART probe with Z-gradient, acquired the high-field NMR data. By default, phase cycling on a Bruker spectrometer results in the selection of only a single coherence pathway. To implement the DCCT schema, we present a robust

template for saving all transients of a phase cycle in listing A.2.

III.4. Software Strategy

The pySpecData library, developed in part for this work, plays a crucial role in the software strategy deployed here. Aside from storing data in an object-oriented format (with a structure not dissimilar to the xarray library [51]), pySpecData offers key advantages for spectroscopic data.

As a specifically relevant example, most of the methods presented here require treatment of the phase cycle as an additional dimension of the data, beyond the standard direct and indirect dimensions. To avoid confusion tracking the meaning of the multiple dimensions (*e.g.*, whether the 1^{st}, 2^{nd}, or 5^{th} dimension encodes phase cycling at a particular point in the code), pySpecData utilizes modern object-oriented capabilities. Specifically, the class of objects designed for storage of data includes a "label," along with optional units and axis coordinates, associated with each dimension. It also incorporates methods for addressing and selecting the data with compact notation and for performing common operations such as Fourier transformation. As a result, relabeling a time axis (such as centering an echo about $t = 0$) automatically leads to an appropriate frequency-dependent phase shift upon Fourier transformation. It also enables automatic dimensional alignment and creation that facilitates, *e.g.*, vectorized computation of cost functions by easily introducing new dimensions corresponding to different choices of optimization parameters. Other benefits include (1) uniform storage and processing of data both from proprietary file formats and directly acquired from instruments, (2) automatic interpretation of symbolic functions supplied for fitting (including the identification of fitting parameters *vs.* data coordinates), and (3) automatic propagation of errors. An important observation reported here is that the spectroscopist can capitalize not just on the object-oriented organization of data and associated information, but also on the more singularly object-oriented capabilities of the Python programming language such as operator overloading and property definitions.

IV. Results

While advancing the ODNP methodology, the authors noted a need for a sweeping reevaluation of basic elements of NMR acquisition and data processing along several fronts. Although various ad-hoc solutions have been developed over the years, this work focuses on addressing the lack of a consistent, modern, and well-explained schema (approach, plan, and organization) for presenting and optimally processing all the raw data acquired during an ODNP experiment (and, more generally, NMR techniques under active development). Conceptually, this strategy for data manipulation and visualization integrates the synergistic benefits of three techniques: (1) domain coloring for visualizing complex data [52], which removes the need for phase correction before data can be interpreted, and (2) object-oriented capabilities that facilitate the treatment of new dimensions introduced to store all the information in a phase-cycled experiment, as well as Fourier transform operations, and (3) open-source libraries that aid in visualization.

In the following text, Sec. IV.1 first demonstrates how domain coloring can provide a compact representation of NMR signal phase. Formal implementation of "phase cycling dimensions" as additional dimensions in an NMR dataset yields a variety of benefits, starting with the rapid setup and optimization of the NMR experiment and instrumentation (Sec. IV.3.A). A visualization of standard nutation curve data provides a straightforward introduction to this non-standard plotting technique (Sec. IV.3.B). Notably, a simultaneous presentation of all (distinguishable) coherence transfer pathways, which typically have different signal phases or timings, in a domain-colored format proves surprisingly useful. We refer to the resulting image as a "DCCT map," alluding to the term 'CT map' in the seminal literature [25]. While traditional techniques involve throwing out at least some data (undesired CT pathways, the imaginary part of data, *etc.*), DCCT maps provide a comprehensive overview of all acquired data in one image, visualizing the relationship between signal in the desired coherence pathway and correctly separated artefacts, as well as signal improperly sorted into undesired CT pathways. This manuscript refers to these three contributions, respectively, as: "desired signal" or "desired pathways," "artefacts" or "artefactual pathways," (Sec. IV.3) and "phase cycling noise" (Sec. IV.3.C). In the results that follow, DCCT maps enrich signal analysis to inform experimental design and the development of data-processing algorithms (Sec. IV.4), without adding any additional time cost to a more traditionally-acquired NMR experiment.

IV.1. Display of Signal Phase

Before considering the visualization of signal in the coherence domain, this manuscript first tests the applicability of the domain coloring concept to raw NMR data (*i.e.*, data that may be Fourier transformed, but without any type of phasing/timing corrections or other post-processing). Domain coloring plots appear in other fields: *e.g.*, in solid state physics studies, hue frequently represents directionality [53, 54]. Similarly, several public-domain webpages present example diagrams illustrating phase with hue. Nevertheless, such plots remain underexploited in MR data visualization [55, 56]. As indicated in Fig. 2a, hue corresponds to the complex phase and value/intensity corresponds to the complex magnitude. The Matplotlib Python plotting library [57] specifically enables the development of libraries such as pySpecData to deploy a wide variety of such custom plotting styles with relative ease. Armed with this plotting technique, the spectroscopist can assess the success of an experiment at a glance, without requiring any phase or timing corrections.

A 390 µL (Ni^{2+}-doped water) sample inside a solenoid

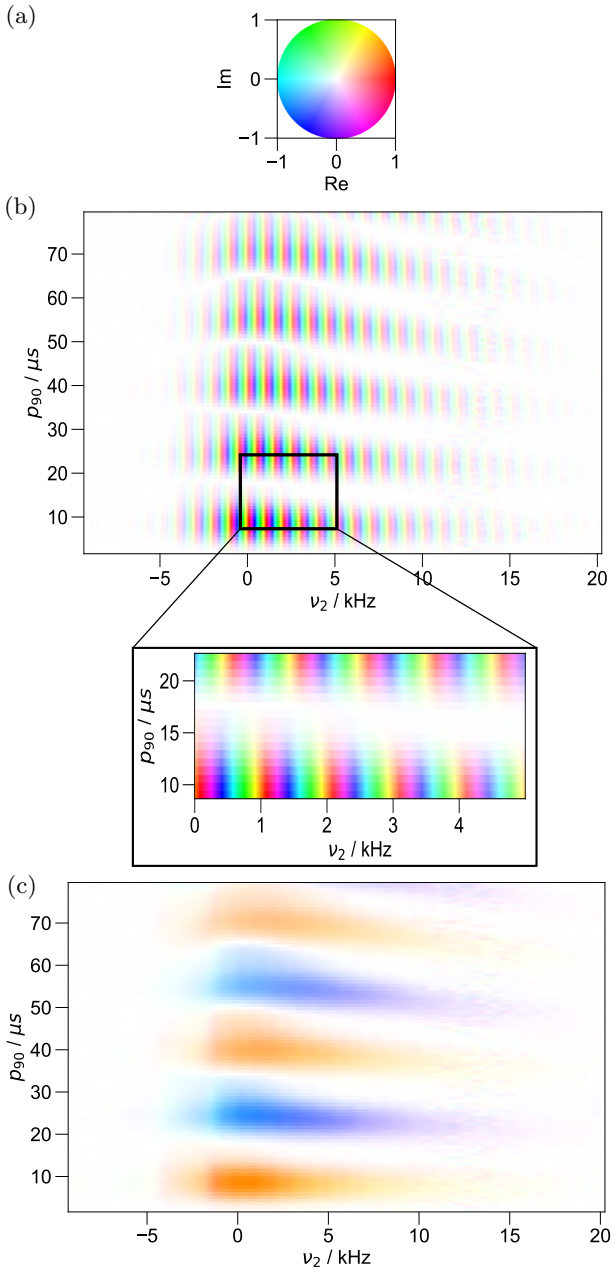

FIG. 2. (a): The coloring of data in the complex plane used in the DCCT map, where intensity indicates magnitude, and color indicates phase. (b) The raw signal from an echo-based nutation curve after selection of the appropriate coherence pathway. Frequency-dependent phase shifts manifest in the domain coloring display as a rainbow banding (inset), here with a periodicity of 5 cyc/5 kHz = 1 ms. When zoomed out, the image may appear grey, which indicates a rapid variation in colors (phases) in the grey area. The sudden change in color from bottom to top along any particular column as the signal passes through a faint patch (amplitude near zero) indicates the inversion of the signal along the indirect dimension. (c): Application of the 1 ms time shift yields coherently phased signal.

coil probe provides the signal for this section. As mentioned previously, this sample size experiences a much greater range of field inhomogeneity than a probe with a capillary sample. Fig. 2b illustrates the raw signal (no phasing corrections), from the desired CT pathway of an echo-based nutation curve (pulse sequence: θ–τ–2θ–*acq.*, with tip angle $\theta = \gamma B_1 p_{90}$ increasing along the indirect dimension). The inset of Fig. 2b shows all frequencies where the pulse excites signal while also clearly demonstrating the inversion of the signal as θ passes through 180°. During inversion, the signal passes through zero (white) while also changing color to indicate the 180° phase change (*e.g.*, red to cyan or blue to yellow, or *vice versa*). A quick glance at a complex domain coloring plot can ascertain information that may otherwise require a(n inverse) Fourier transform and separate plot in order to be understood. For example, a time-shift appears in the frequency-domain plot as a "rainbow" color variation, and in the case of a spin echo, indicates that the origin of the time axis ($t = 0$) does not properly align with the center of the echo signal. Here, an inspection of Fig. 2b (inset) indicates 5 cycles (10π rad) of phase rotation over a span of 5 kHz, corresponding to a time shift of 1 ms.

Fig. 2c introduces this 1 ms timing/phase correction, achieved by shifting the time axis in the pySpecData processing code (as in listing A.4) or, equivalently, applying the appropriate first-order phase shift in the frequency domain. As expected from an echo signal properly centered about $t = 0$, Fig. 2c yields a uniform phase lineshape.

Fig. 2 provides just one of many possible examples in which domain coloring plots both quickly guide simple manual data processing of raw data and also allow instant access to information. Note how a real-valued plot of Fig. 2b would generate ambiguity between the phase variation and amplitude variation. Here, a simple glance reveals phase variation along the direct dimension and amplitude variation along the indirect dimension. Also note that information such as the time delay of the signal is accessible in both domains (time and frequency), while other plotting strategies might make this information apparent in only one domain.

IV.2. Treatment of Phase Cycling

As demonstrated in this and the following subsections, the incorporation of many short dimensions corresponding to the cycling of individual pulses clearly illustrates the effects of drifting fields, rf amplitude misset, resonance frequency offset effects, and pulse ringdown. It also yields a simple scheme for quantifying the SNR ratio.

With the increased practicality offered by object oriented programming in hand, the original conceptual approaches to phase cycling – pioneered by Wokaun, Bodenhausen, Ernst, and others – assume new meaning; these approaches incisively focus on the concept that the change in coherence order during a pulse (Δp) is, quite

simply, the Fourier transform of the dimension along which pulse phase is cycled (φ_j, Eq. (2)) [25, 29, 58]. While the traditional schema adds up the effect of all pulse phase variations to determine the overall phase cycle of the desired coherence pathway, the DCCT schema keeps matters simpler by treating each pulse involved in the phase cycle separately. To achieve this, the processing code organizes data into one or more short (typically 2-4 elements long) dimensions for each pulse involved in the phase cycling, in addition to the traditional direct (t_2) and indirect dimensions typical of multidimensional NMR experiments. Each of these phase cycling dimensions can be in the "phase cycling domain" (φ_i for pulse i) or the conjugate "coherence transfer domain" (Δp_i). More typical phase cycling procedures effectively filter and discard these additional dimensions. However, a central result presented here is that modern instrumentation and open-source coding [57, 59, 60] standards facilitate both this treatment of the phase cycle as an additional dimension and the ability to visualize these new dimensions with automatically generated DCCT maps. Together, these offer a more comprehensive view of the underlying spin physics and of the impacts of experimental imperfections.

IV.3. Domain Colored Coherence Transfer (DCCT) Schema

Developing new methods under adverse circumstances, such as new ODNP instrumentation or protocols, requires unambiguous identification of signal as well as quick insight into any potential issues with the setup. The DCCT map, importantly, displays the artefactual signal arising from undesired coherence pathways. Instrumental errors that lead to imperfections in the phase cycle itself can lead to miscategorization of the desired signal as arising from undesired pathways–resulting in signal loss and distortion, or miscategorization of artefactual signal as arising from the desired coherence pathway–leading to artefacts in the final result. By displaying these features, DCCT maps provide greater insight into the effects of experimental imperfections on the signal. These are most easily demonstrated through a series of examples.

IV.3.A. Example: Phase-cycled NMR with Standard Test + Measurement Equipment

Non-specialized test and measurement equipment can acquire a reasonable NMR signal [61]. The DCCT schema enables rapid setup and diagnosis of such "bare bones" NMR instrumentation. For example, here, an arbitrary function generator operates as an rf source and a digital oscilloscope operates as a digital to analog converter whose bandwidth and sampling rate exceed the bandwidth of an attached analog low-pass filter (Sec. III.2.C). Such an inexpensive, uncomplicated NMR spectrometer is invaluable for diagnostic purposes – *e.g.*, when assembling a modular ODNP spectrometer.

Object-oriented Python code [60] controls both the function generator and the oscilloscope via USB 2.0 communication, an instrumental setup similar to that which was described previously [62] (see listing A.5). Despite the fact that a standard oscilloscope has no built-in phase-cycling capabilities, the software can trivially save separate transients acquired with different pulse phases, along with the pulse waveform as a phase reference. The object-oriented code implemented here frequency filters the results, digitally mixes down and phase references by comparison to the captured pulse waveform, and saves data in an HDF5 format. For a spin echo experiment, as in Figs. 3 and 4, it stores the data immediately available from the acquired transients in a 3-dimensional array of data, with shape $n_{\varphi_1} \times n_{\varphi_2} \times n_{t_2}$, representing the function $s(\varphi_1, \varphi_2, t_2)$ [63]. Here n_{φ_1} and n_{φ_2} are the number of phase cycling steps for the two pulses, and n_{t_2} is the number of time points along the direct dimension.

After 3-dimensional Fourier transformation (without zero filling) along the φ_1, φ_2, and t_2 dimensions, the signal becomes:

$$\tilde{s}(\Delta p_1, \Delta p_2, \nu_2) = \iiint e^{-i2\pi(\nu_2 t_2 + \Delta p_1 \varphi_1 + \Delta p_2 \varphi_2)} \times f_{sampling}(\varphi_1, \varphi_2, t_2) \times s(\varphi_1, \varphi_2, t_2)\, d\varphi_1 d\varphi_2 dt_2 \tag{33}$$

where Δp_j indicates the coherence change during pulse j, ν_2 gives the offset frequency (in Hz) along the direct dimension, and $f_{sampling}$ gives the function representing the instrumental and/or digital filtering and discrete sampling of the otherwise continuous signal (see SI-A for further notes). As a reminder, the coherence level change (Δp_i) and the cycled pulse phase (φ_i) are Fourier conjugates (Eqs. (2) and (33), see example code listing A.6).

Fig. 3 presents the DCCT map that results from an initial attempt at finding signal with a spin echo pulse sequence (Fig. 3a), as well as an optimized attempt (Fig. 3b). In both Fig. 3a and Fig. 3b, the CT pathways $\Delta p_1 = +1$ and $\Delta p_2 = -2$ contain signal unambiguously identified as arising from the spin echo. Coherence pathways that are not physically meaningful are marked with an X – *e.g.*, in Fig. 3, the coherence order change marked by the first pulse, Δp_1 has been marked with an X due to the fact that the initial pulse acting on polarization only generates single quantum coherence here. On the other hand, when several reasonable Δp values are Fourier aliased together, all such values are presented, separated by commas.

In this example, the DCCT map clearly demonstrates that, despite the non-specialized instrumentation employed here, the phase cycling of the pulses on the function generator and phase referencing of the oscilloscope operate as expected, giving clean isolation of the CT pathways. Furthermore, the sign associated with the phases can vary on different spectrometers from different manufacturers, as previously noted, [64, 65], and this is observable in the DCCT map. In Fig. 3, the conven-

tion is properly applied, but an inversion of the sign of Δp (indicating an inversion of the sign of φ) could be easily observed and corrected.

Notably, Fig. 3a identifies that the majority of the coherences generated by the pulse sequence do not contribute to the spin echo (green solid line, Fig. 3c), but rather to undesired/artefactual signal, where the second, longer pulse (nominally the 180° pulse) excites an FID ($p = -1$) directly from the polarization ($p = 0$) (blue dashed line, Fig. 3c). The DCCT map, therefore, offers insight into experimental improvements by identifying the different pathways where the polarization has been utilized. In this simple example, after increasing the length of both pulses, the pulse sequence predominantly generates coherences that contribute to the spin echo signal. At the same time, the rainbow banding in the time domain data of Fig. 3a, also indicates that the resonance frequency differs significantly from the carrier frequency. Fig. 3b corrects both the 90-pulse time and the carrier frequency to yield an intense, single-colored band in the desired CT pathway for the echo signal.

Note that artefacts due to pulse ringdown cycle with the same phase as the pulses, in the $\Delta p = -1$ pathway for the relevant pulse, *i.e.*, in $\Delta p_1 = 0 \rightarrow \Delta p_2 = -1$ and $\Delta p_1 = -1 \rightarrow \Delta p_2 = 0$. These artefacts overlay with simple (FID-like) excitation and appear here as regions of alternating signal (colored) and no signal (white), with the latter arising from times where the oscillating high-intensity ringdown saturates the duplexer diodes and/or low-noise amplifier. Thus, with a single phase-cycled scan, the data can highlight how spin echo acquisition gives uniquely unambiguous confirmation that true signal has been observed.

The DCCT schema introduces the DCCT map as an intermediate step between acquisition and presentation of the final data in a traditional phase cycled NMR experiment. The DCCT schema also opens up the possibility of other plots that display a subset of the data offered by the DCCT map, tailored to particular experiments. For example, after plotting Fig. 3, extraction of a subset of the data in a customized plot yields Fig. 4, which serves to emphasize the strong preference for echo-based detection for this large sample, due to the rapid T_2^*. Meanwhile, traditional NMR acquisition employing on-board signal averaging through a phase-cycled receiver would select an even more exclusive subset of the available information, detecting and saving exclusively the signal from the desired echo CT pathway $\Delta p_1 = +1 \rightarrow \Delta p_2 = -2$ (the blue line in Fig. 3c); the resulting data would only indicate the presence or absence of signal.

IV.3.B. Example: Nutation Curve

In these results, a SpinCore RadioProcessorG replaces the USB 2.0 function generator and oscilloscope to enable faster rates of data transfer to the computer, as well as the use of digital filtering and downsampling that permit the distortion-less capture of longer signals [66].

The same spin echo nutation experiment from Fig. 2

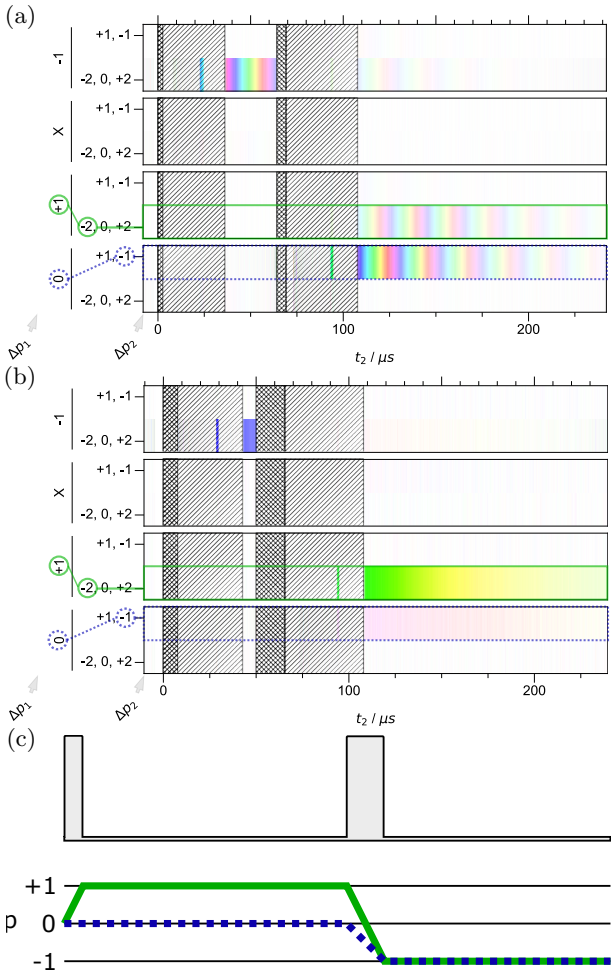

FIG. 3. Spin echo acquired by an NMR spectrometer constructed from off-the-shelf test and measurement equipment for 13 mM $NiSO_4$-doped water (a) under suboptimal experimental parameters and (b) optimal parameters. The data distinctly peaks around 120 µs at the expected location in the coherence transfer domain – specifically, the $\Delta p_1 = +1$, $\Delta p_2 = -2$ pathway where Δp_n is the Fourier conjugate of the pulse phase (φ_n) dimension. The receiver deadtime extends to approximately 35 µs after the center of the 180° pulse. Low-B_1 regions of the sample contribute to the subtle signal visible at $\Delta p_1 = 0$ $\Delta p_2 = -1$, which is an FID arising from the second pulse.

offers more information when presented as a DCCT map (Fig. 5). The full dataset comprises a 4-dimensional function, $s(t_p, \varphi_1, \varphi_2, t_2)$, with a size of $n_{t_p} \times n_{\varphi_1} \times n_{\varphi_2} \times n_{t_2} = 100 \times 2 \times 2 \times 1024$. A 3D Fourier transform converts s to $\tilde{s}(t_p, \Delta p_1, \Delta p_2, \nu_2)$. The DCCT map demonstrates all possible conversions of the polarization to coherent signal (here both echo-like and FID-like), at all frequencies where it occurs, while simultaneously preserving all relative phase/sign information. Here, domain coloring proves crucial, given that signal from different coherence pathways occurs at different times and with different absolute phases. For example, Fig. 5 represents data from an early trial on a modular system with new components,

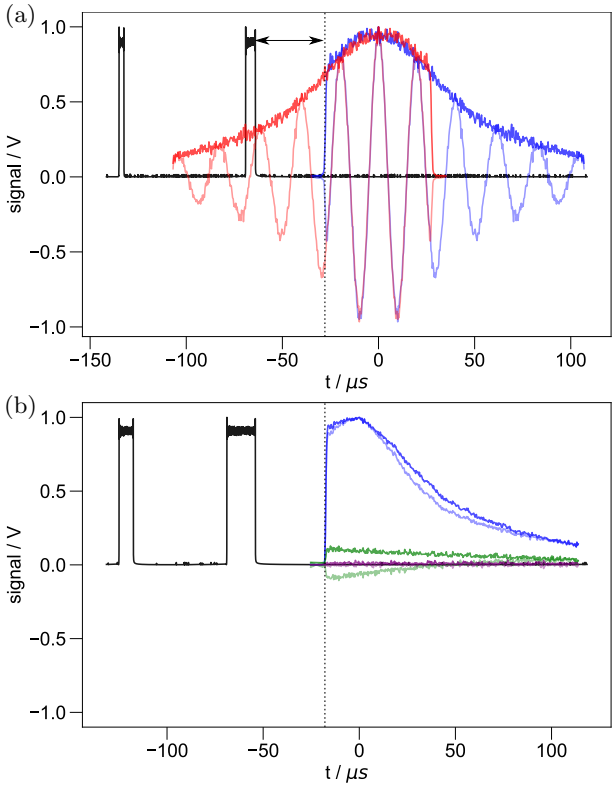

FIG. 4. (a): The subset of signal from Fig. 3a that follows the echo coherence pathway of Fig. 3c is shown, with the complex magnitude of the pulse waveform (black) and signal (blue, with the real part in fainter blue) captured by the oscilloscope shown as 1D line plots and with $t = 0$ set to the echo center. A comparison to the Hermitian conjugate of the signal (red) clearly illustrates the time at which the signals diverge. Due to T_2^* (inhomogeneous) decay over the timescale of the deadtime (dashed black vertical line, 35.7 µs), the signal loses some 25% of its amplitude. In (b), the pulse length has been optimized and the carrier frequency set on resonance, showing the echo pathway (blue), the residual FID pathway (green), and the pathway which should not contain any signal (purple). Here, the echo pathway is much more intense than the unwanted FID pathway.

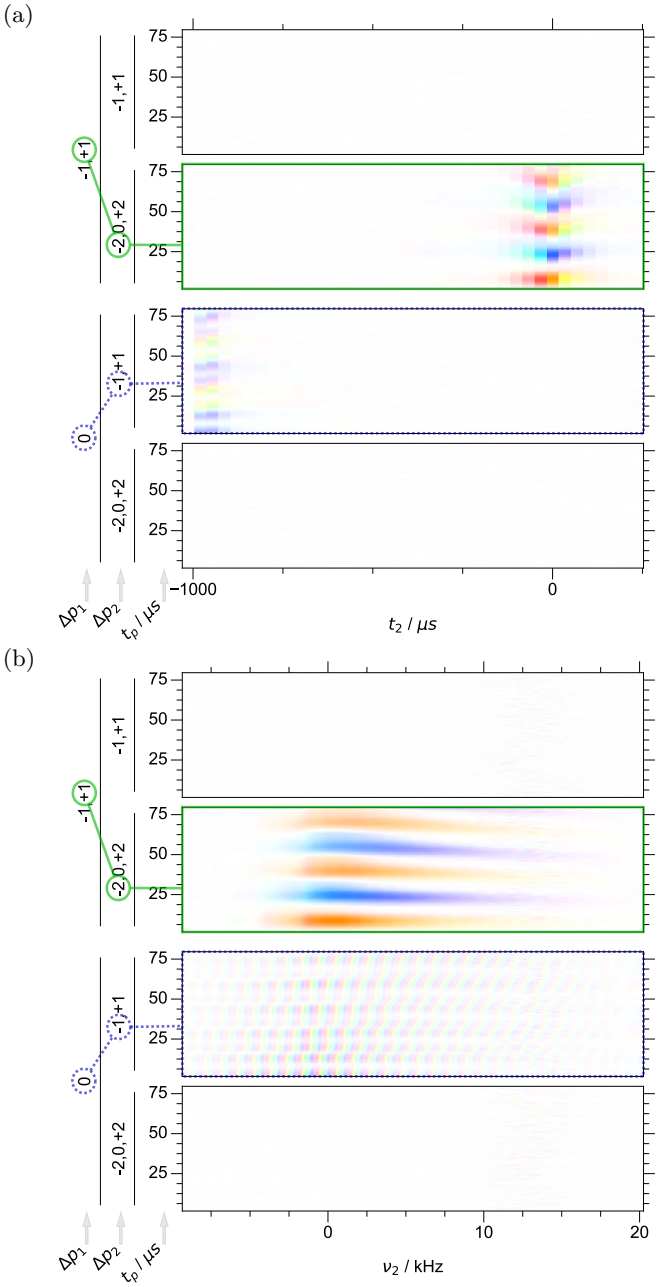

FIG. 5. Full DCCT map from a (t_p pulse)-(τ delay)-($2t_p$ pulse) sequence, where $t_p = 2 - 80$ µs and $\tau = 1$ ms in both the (a): time domain and (b): frequency domain . The green boxes outline the echo CT pathway (presented exclusively in Fig. 2), while the dotted blue boxes outline the FID-like CT pathway. These pathways follow the coherence diagram outlined in Fig. 3c alongside the pulse sequence. The only adjustments made to the raw data are (1) slicing to a frequency bandwidth where signal is observed and (2) setting $t_2 = 0$ to the maximum of the echo coherence pathway.

and it was unclear if the phase cycling was functioning optimally. The DCCT map highlights the contribution of an unwanted signal artefact (blue-dashed line in Fig. 5) that, in the absence of a phase cycle, would interfere with the desired signal (solid green line) It clarifies that simple hardware and data processing are capable of cleanly separating this artefact from desired signal. Fig. 5 demonstrates another general advantage of the DCCT map: the same information may be displayed and interpreted in either the time (Fig. 5a) or the frequency (Fig. 5b) domain. Specifically, note how the appearance of FID-like (blue dashed) and echo-like (green solid) signal at two different times in the time domain can be deduced directly from the rainbow banding of the FID-like signal in the frequency domain, in contrast to the constant color of the echo signal.

IV.3.C. Example: Field Instabilities and the Estimation of Noise

Another example of relevance to ODNP arises when considering field instabilities. The Bruker ESR system

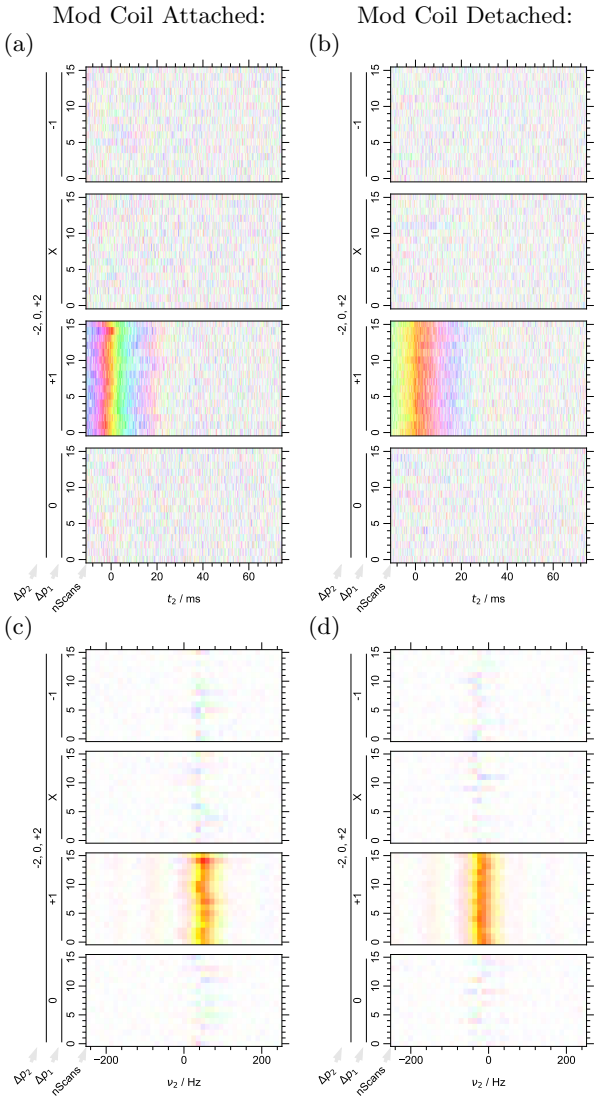

FIG. 6. Attaching vs detaching the ESR modulation coil allows for a controlled test of 2 situations with different field stability, as shown for both the time domain ((a) and (b)) and frequency domain ((c) and (d)), respectively. Three notable effects include the variation of the average frequency, increased amplitude of the signal in inactive coherence transfer pathways elements of the coherence dimension, and variation of the echo center. With the mod coil detached (d), the average signal value in the desired coherence pathway is 1.04× that with the mod coil attached (c), while the root mean squared amplitude of the noise in all other (*i.e.*, inactive) coherence pathways decreases by a factor of 0.86. Therefore, while the signal amplitude remains roughly equivalent, detaching the mod coil leads to a noticeable decrease in artefacts linked to improper phase cycling (variation of static field's magnitude or time dependence from one step of the phase cycle to the next).

comes equipped with a system for generating a standard modulation field (typically varying with a period of 10 µs), and one practical concern of ODNP spectroscopy involves what influence this might have on the NMR signal (when the spectrometer is set to "standby" mode). While a specific practical interest related to ODNP motivates this measurement, it also, more importantly, provides a controlled demonstration of general effects arising from unstable fields. The DCCT maps in Fig. 6 represent signal from a spin echo experiment comprising an 8-step phase cycle with 16 repeats, when the modulation cable is left attached to the cavity (Figs. 6a and 6c) *vs.* when it is detached from the cavity (Figs. 6b and 6d).

The timing and phase of the echo in Figs. 6a and 6b vary from scan to scan, as evidenced by, respectively, the left *vs.* right translation of the echo position relative to the x-axis and change to the color of the signal at $t = 0$. Notably, domain coloring helps to emphasize these concurrent variations. Again, the frequency domain DCCT maps (Figs. 6c and 6d) make the same effect evident in a different form: as changes in how the color varies from left to right across the spectrum and in the average (overall) color across the spectrum for each scan. As expected, the signal remains more stable when the connector for the modulation coil is disconnected, as in Figs. 6b and 6d.

The echo signal responds to the increased field variation from the modulation coil in three specific ways. First, as already noted, the phase (color) of the signal at $t = 0$ (or across all frequencies) varies more across consecutive scans. This inconsistency arises from the residual modulation field driving changes in the B_0 field strength before *vs.* after the 180° pulse. This scan-to-scan variation of the signal phase would lead to reduced signal amplitude if these scans were averaged. Second, greater frequency variation of the individual transients contributing to the signal in Fig. 6c (also evident from the differences in the rainbow banding of Fig. 6a) results in the more jagged appearance of the signal "bands" as compared to Fig. 6d. If the various scans of Fig. 6c were averaged together, a distorted lineshape with increased linewidth and reduced signal energy and amplitude would result, underscoring the usefulness of interrogating the impact of each transient. Third, and perhaps most significantly, in both cases, the DCCT map shows noise/artefacts in the CT pathways outside the echo-like ($\Delta p_1 = +1$, $\Delta p_2 = -2$) pathway. These artefacts are concentrated within the signal bandwidth. No explanation based on the transitions between different coherence levels of the density matrix can rationalize the appearance of significant artefactual signal in these "inactive" CT pathways shown in Fig. 6. Rather, since the phase cycle must be sorting signal into the wrong CT pathway, we refer to the noise-like artefacts that appear in the inactive pathways as "phase cycling noise." The difference is subtle, but with the modulation coil attached, more intense spikes in the phase cycling noise are observed, as can be quantified from the mean squared phase cycling noise amplitude (1.3× higher with the modulation coil attached).

Clearly, ODNP should be acquired with the modulation coil detached under all cases. Even then, because the signal energy is diverted into energy for phase cycling

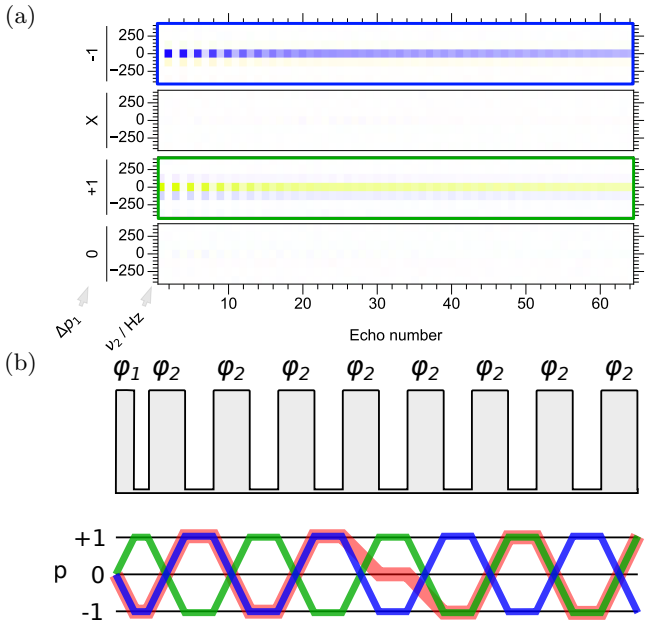

FIG. 7. DCCT map presentation of CPMG data acquired at 15 MHz with a 4-step phase cycle of the initial excitation pulse (a) and an independent 4-step phase cycle of all 180° pulses in concert. Here, the x-axis corresponds to the echo number, while the direct dimension within each echo window appears as the innermost dimension along the y-direction. For simplicity, the single element of the $\Delta p_1 + \Delta p_2$ dimension that contains valid signal ($\Delta p_1 + \Delta p_2 = -1$) has been selected. Detected signal alternates between two coherence pathways $\Delta p_1 = 1$, $\Delta p_1 + \Delta p_2 = -1$ (green) and $\Delta p_1 = -1$, $\Delta p_1 + \Delta p_2 = -1$(blue) with each π pulse. Beginning with the 6^{th} or 7^{th} π pulse, signal 'bleeding' from the alternate pathway, as shown in (b), starts to become significant. The red line gives one example of the many pathways that, cumulatively, give rise to such "bleeding."

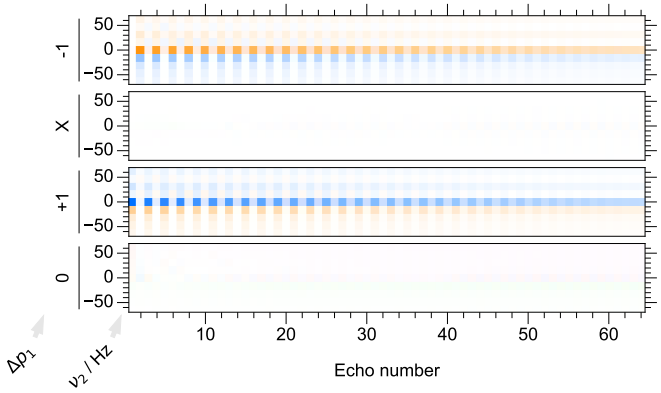

FIG. 8. CPMG data was acquired on high-field (400 MHz) Bruker spectrometer for 64 180° pulses. After each 180° pulse, the signal alternates between $\Delta p_1 = +1$ and $\Delta p_1 = -1$ until eventually bleeding is observed (by around the 12^{th} echo).

noise (Sec. II.1.F), the standard deviation across the coherence domain provides an appropriate source for error bars on datapoints in the spectrum. However, it will be noted that care must be taken when applying these errors to integrated signal, since they can be correlated.

IV.3.D. Example: CPMG

As noted in other publications, ODNP can be acquired with a CPMG (Carr-Purcell Meibloom-Gill) sequence, as is typical of many studies in low-field and portable MR [8, 10, 67]. An interesting result of the DCCT map arises when applied to a fully phase cycled CPMG – that is, a four step phase cycle on a 90° excitation pulse, followed by a train of evenly spaced 180° pulses, phase cycled in concert. Some analysis schemes bin the results of the phase cycle into a "CP" component, where the phases of the 90° pulse match the phase of the 180° pulses or have a 180° phase difference, and a "CPMG" component, with orthogonal phases. Since the DCCT map offers a new means for visualizing signal, it provides the opportunity to revisit the decay of CP components and the persistence of CPMG components [68]. Briefly, following the DCCT treatment, signal should alternate between $\Delta p_1 = +1$ and $\Delta p_1 = -1$, as in the initial echoes of Fig. 7a; however, signal starts to "bleed" into the opposite Δp_1 value following pathways like those shown in Fig. 7b, ultimately yielding a constant signal for both values of Δp_1. This corresponds to the previously observed decay of the "CP" component [68], viewed from a new perspective. This example also allows the introduction of phase and coherence dimensions that group the effects of more than one pulse.

In more detail, naively following the methodology laid out in Sec. IV.1, the software can sort the data into a 4D dataset (a single-line command in pySpecData), with the signal given by the discretized function $s(\varphi_1, \varphi_2, \tau_{echo}, t_2)$ of shape $n_{\varphi_1} \times n_{\varphi_2} \times n_{\tau_{echo}} \times n_{t_2}$; where t_2 gives the points within each echo and τ_{echo} gives the center position of each echo. It then Fourier transforms the signal along the φ_1, φ_2, and t_2 dimensions to permit filtering by resonance frequency and coherence pathway.

The initial (nominal) 90° pulse changes the coherence order of the initial polarization by $\Delta p_1 = \pm 1$. Here, since the 180° pulses are phase cycled together, Δp_2 refers to the net change in coherence order due to all 180° pulses. Therefore, odd-numbered echoes harvest signal from the pathway that experiences $\Delta p_1 = +1$ and $\Delta p_2 = -2$. In contrast, even-numbered echoes harvest signal from the pathway that experiences $\Delta p_1 = -1$ and $\Delta p_2 = 0$.

Thus, the CPMG experiment particularly motivates an informed choice of phase cycling dimensions that simplifies the analysis. Specifically, since only two types of pulses are phase cycled (along dimensions φ_1 and φ_2), a coherence-domain dimension $\Delta p_1 + \Delta p_2$ only yields signal for $\Delta p_1 + \Delta p_2 = -1$. The only signal that appears for other values of $\Delta p_1 + \Delta p_2$ arises from instrumental artefacts. A rearrangement of the expression $\Delta p_1 \varphi_1 + \Delta p_2 \varphi_2$ (which is the effect of phase cycling on the phase angle

of the transients) yields

$$\Delta p_1\varphi_1 + \Delta p_2\varphi_2 = \Delta p_1\left(\varphi_1 - \varphi_2\right) + \left(\Delta p_1 + \Delta p_2\right)\varphi_2, \tag{34}$$

and motivates rearranging the signal to the form $s(\varphi_1 - \varphi_2, \varphi_2, n_e, t_2)$ whose (3D) Fourier transform is given by $\tilde{s}(\Delta p_1, \Delta p_1 + \Delta p_2, n_e, \nu_2)$ where n_e represents the echo number.

The Δp_1 dimension disentangles the pathways that should give rise to the even *vs.* odd echoes. Odd-numbered echoes (following 1, 3, *etc.*, inversion pulses) should only present signal for $\Delta p_1 = +1$ since the expected/desired coherence pathway with $\Delta p_1 = +1$ (green line in Fig. 7b) only reaches $p = -1$ for odd echoes. Analogously, even-numbered echoes should only present signal for $\Delta p_1 = -1$ (blue line in Fig. 7b). The observed signal shown in the DCCT map of Fig. 7a derives from the alternating green and blue lines along the $p = -1$ coherence level. In this scheme, as long as even *vs.* odd echoes remain separated along Δp_1, any phase encoded between the excitation and first echo pulse would be properly preserved.

However, due to offset or misset effects, imperfect 180° pulses can store a small fraction of transverse magnetization along the z-axis for one or more echo periods and then re-excite it as observable magnetization (the red pathway in Fig. 7). In Fig. 7b, the signal cleanly separates into the desired coherence channels for the first few echoes. However, near the 7$^{\text{th}}$ echo, significant amounts of $\Delta p_1 = +1$ signal begin to appear in even-numbered echoes, as well as significant amounts of $\Delta p_1 = -1$ signal in odd-numbered echoes – *i.e.*, the signal "bleeds" from the even echo pathway into the odd echo pathway, and *vice versa*.

Fig. 7a also demonstrates that signal from the two Δp_1 pathways can be combined into a single decay with coherent phase by subtracting (adding with a phase rotation of 180°) the $\Delta p_1 = -1$ signal and the $\Delta p_1 = +1$ signal. Such an operation reduces to:

$$\begin{aligned}
&\frac{1}{2}\left(\tilde{s}(t_2, +1) - \tilde{s}(t_2, -1)\right) \\
&\quad = \frac{1}{2}\sum_{n=0}^{3}\left((-i)^n s\left(t_2, \frac{n}{4}\right) - (i)^n s\left(t_2, \frac{n}{4}\right)\right) \\
&\quad = -is\left(t_2, \frac{1}{4}\right) + is\left(t_2, \frac{3}{4}\right)
\end{aligned} \tag{35}$$

where s is a function of t_2 and $\varphi_1 - \varphi_2$, and $\tilde{s}$ a function of t_2 and Δp_1, where n gives the integral steps of $\varphi_1 - \varphi_2 = \frac{n}{4}$, and where the second line uses the standard identity $e^{\frac{n\pi}{2}} = i^n$ in conjunction with Eq. (2), and where the third line keeps only the surviving terms of the sum. Thus, subtracting signal from the $\Delta p_1 = +1$ and -1 pathways is mathematically equivalent to adding the two CPMG components ($\varphi_1 - \varphi_2 = \frac{1}{4}, \frac{3}{4}$ cyc). Similarly, a sum of the $+1$ and -1 pathways – equivalent to isolating the CP ($\varphi_1 - \varphi_2 = 0, \frac{1}{2}$ cyc) component – would cancel out the long-lived tails of the signal, which are 180° out of phase. Thus, interestingly, the "CP" *vs.* "CPMG" components of the signal arise naturally from this analysis as the Fourier conjugate of Δp_1, the $\varphi_1 - \varphi_2$ dimension. Specifically, transients for which $\varphi_1 - \varphi_2 = 0$ cyc or $\frac{1}{2}$ cyc (π rad) are the "CP" component and those for which $\varphi_1 - \varphi_2 = \frac{1}{4}$ cyc or $\frac{3}{4}$ cyc ($\frac{\pi}{2}$, $\frac{3\pi}{2}$ rad) are the "CPMG" component.

In the case where field inhomogeneity is much smaller than the B_1 multiplied by the number of echoes ($\Delta\Omega \ll |\gamma B_1 n_{echo}|$), both CP and CPMG signals present a significant amplitude [68]. The "bleeding" observed here illustrates the oscillation and decay of the CP-component [68] arising from unanticipated storage of coherence along z (the red line in Fig. 7b) and clearly indicates when phase encoding information is not valid. Because only magnetization orthogonal to the direction of the pulse field in the rotating frame (*e.g.*, x-magnetization subjected to a y-pulse) is stored along the z-axis, this affects only the CP transients of the phase cycle, and not the CPMG transients. The resulting loss of phase-sensitive information, in turn, demands the application of an alternate acquisition scheme for many applications [68]. However, for various reasons, one may wish to harvest as much phase information as possible from the standard pulse sequence, while optimizing the SNR. Here, the DCCT map offers guidance on optimally filtering the signal. In the most rudimentary case, this involves zeroing the even/odd echoes of each pathway that contain only noise and frequency filtering along ν_2. This corresponds to preserving some information arising from the CP component

The DCCT schema may also be applied to a CPMG measurement on a high-field spectrometer (Fig. 8). Here, the bleeding occurs at a later echo number due to the greater homogeneity of the superconducting magnet, pointing to the possibility of utilizing phase information as long as the number of echoes is kept limited.

Finally, note that these results represent examples where the phase cycling is constrained to a 90° step. Notable examples in the literature, such as the PIETA sequence, can maximize the use of concurrent phase cycles of multiple pulses for cases where finer-level phase incrementation is possible (and where DCCT coding and visualization should also prove fruitful) [28].

IV.4. Algorithms Motivated and Analyzed by DCCT

The remaining results introduce several realistic examples of how the DCCT map visualizes the transformation of the data from raw signal, through phasing and alignment, and ultimately through integration of the real part of the signal. Importantly, the DCCT schema provides a means for organizing and visualizing the data that enables the validation, implementation, and optimization of these algorithms for the purpose of analyzing ODNP data. Here, Sec. IV.4.C, IV.4.D and IV.4.F are specifically attuned to acquiring ODNP data while Sec. IV.4.A, IV.4.B, IV.4.E and IV.4.G should prove of more general interest.

IV.4.A. Phasing of Echo-Detected Signal

In the field of quantitative NMR, various studies have treated the seemingly trivial, but ultimately pervasive and fundamentally linked issues of automated baseline correction and first-order phase correction [43, 69, 70]. The presence of shot-to-shot instabilities of the magnetic field and the desire for a seamless transition between 1D spectroscopy and stroboscopic (*e.g.*, CPMG) acquisition further complicates such attempts. As discussed in theory Sec. II.1.D, echo-based signals can simplify the timing/phase correction of the signal by removing the need to account for the distortion or loss of the first few points in the FID. Specifically, acquisition of echo-based signals replaces the potentially iterative phase and baseline correction with the problem of locating the center of the echo.

Fig. 6a highlights the fact that even when the temporal (left to right) variation of the echo intensity is subtle, the phase (color) of successive echoes varies noticeably. This encourages the use of the full complex signal – *i.e.*, phase as well as magnitude – from as much of the echo as possible in order to identify the echo center.

In fact, a simple algorithm that utilizes the phase information as well as the amplitude information of the echo can generate well-phased baseline-free signal from spin echoes. As a demonstration, a standard sample of water and TEMPOL generated a series of signals as part of a progressive enhancement sequence. Eq. (9) calculates a cost whose minimum locates the center of an echo signal with Hermitian symmetry. Fig. 9a displays this cost averaged across 28 indirect power steps at microwave powers ranging from 0 to 4 W. The cost function exhibits a well-defined minimum at $\Delta t_{min}/2 = 10.6$ms. After subtraction of this value from the time coordinates and application of a uniform zeroth order phase correction to all scans, all signals display approximate Hermitian symmetry. The residual calculated by subtracting the signal from its Hermitian transpose ($s^*(-t)$) barely rises above the level of noise, and the imaginary components of all scans cross zero at $t = 0$ (Fig. 9b). In other words, the detected echo accurately comprises a rising signal ($s_{rising}(t)$) for $t < 0$ and a mirror image (in the sense of Hermitian symmetry, such that $s(t) = s^*(-t)$) FID ($s_{FID}(t)$) for $t > 0$. Under standard electromagnet conditions, the refocusing of inhomogeneities is dramatic with $T_2^* \ll T_2$, and detection of echoes does not lead to a detectable decrease in signal amplitude relative to an FID acquired after a 90° pulse (Fig. SI-1). Finally, FID slicing (Eq. (3)) followed by Fourier transformation gives rise to in-phase, baseline-free signals (Fig. 9c).

Slightly longer echo times are preferred as they allow the spectrometer to acquire a sufficient amount of rising echo signal between the pulse dead-time and the center of the echo. Echo times of as low as 3 ms enable Eq. (9) to easily determine the echo center for 15 MHz NMR. While the timing correction needed may be a conglomerate of various contributions, such as those mentioned in Sec. II.1.D, the system in the authors' lab typically

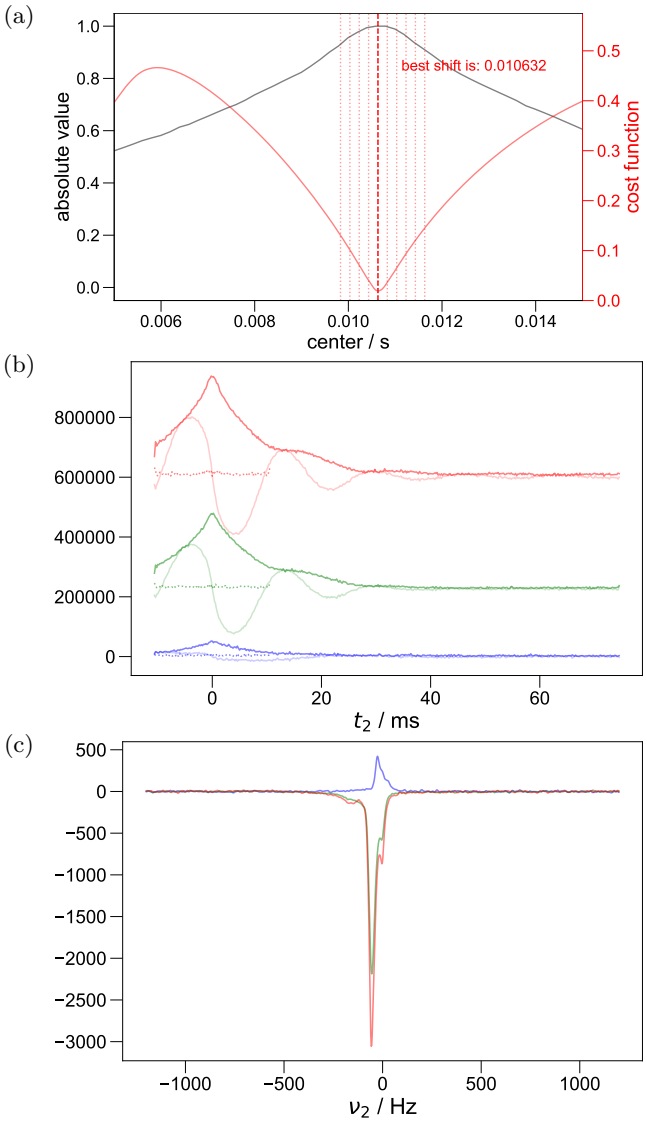

FIG. 9. (a): The cost function Eq. (10) (where $\Delta t/2$ = "center" above) demonstrates a clear minimum at the optimum time shift, $\Delta t_{min}/2$, which represents the precise center of the spin echoes. Subtraction of $\Delta t_{min}/2$ from the time axis centers the echoes at $t = 0$. (b): After applying a uniform zeroth-order phase shift, the imaginary component of the echoes crosses zero at $t = 0$ for all microwave powers employed to measure ODNP enhancement. Subsequent slicing of the FID from these echoes, following Eq. (3), yields well-phased, absorptive, baseline-free signal, the real component of which is shown in (c).

requires a timing correction of 100-500 µs relative to the expected center of the echo ($t_{echo} = \tau + 2t_{90}/\pi$ [37]). Repeated experiments typically reproduce the echo location satisfactorily and enable signal averaging.

IV.4.B. Simple NMR Signal Alignment

Even with a reasonable effort to maintain a stable resonance frequency, significant phase cycling noise tends to appear in the DCCT map of signal acquired on an

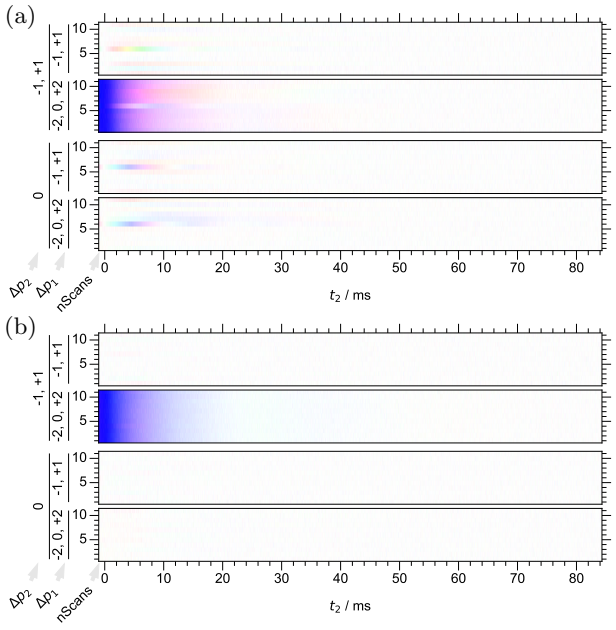

FIG. 10. The DCCT map (time domain) of a spin echo for 10 complete phase cycles with first-order phase correction. The undesired coherence pathways contain a significant amount of phase cycling noise ((a): note especially the 6^{th} scan), which grows in amplitude moving away from $t = 0$ before falling off as the signal phase off. The alignment procedure almost completely mitigates this phase cycling noise (b), as discussed in the text.

electromagnet, as shown in Figs. 11b and 12c. Fig. 10a illustrates the DCCT map of the signal from a simple spin echo with a short (~ 1 ms) echo time on the 15 MHz electromagnet system, repeated for 10 scans (*i.e.*, 10 complete phase cycles) for an aqueous 100 mM TEMPOL. During this relatively short echo time, the field has little opportunity to drift, and the signal refocuses at the echo center ($t = 0$) almost completely and with a consistent phase. The amplitude of the phase cycling noise relative to the amplitude of the signal increases noticeably for times increasingly further away from the center of the echo. This effect matches the expected effect of a transient to transient variation of resonance (field) offset, which does not affect signal at the echo center, but does affect the evolution of signal phase moving away from the echo center. Thus, an initial inspection implies that a significant portion of phase cycling noise results from field fluctuations.

To ascertain the extent to which the presumed drifting of the static magnetic field is the cause of the phase cycling noise in Fig. 10a, the iterative maximization of Eq. (23) (subjected to a Gaussian mask of width $\sigma = 20$ and nonzero only for the coherence pathways $\Delta p_1 = 0$, $\Delta p_2 = -1$ and $\Delta p_1 = 0$, $\Delta p_2 = 0$ Fig. SI-2) determines the frequency shifts required to align the individual transients, leading to the result shown in Fig. 10b. The alignment mitigates the phase cycling noise while improving the consistency of the signal in the desired CT pathway. Thus, the signal alignment of Eq. (29) proves a viable means to address the experimental complications owed to randomly varying offset.

IV.4.C. Example: Inversion Recovery

Fig. 11 shows the data for an inversion recovery experiment at various stages of processing for an aqueous 500 µM TEMPOL solution. First, Fig. 11a shows the "raw" data with two separate phase cycling (φ_1, φ_2) and direct (ν_2) dimensions. This figure has been subjected only to a time-domain Fourier transform and is included here as a conceptual aid: note that viewing data in the phase domain rarely proves more diagnostic than viewing it in the coherence domain. Without requiring any phase correction, Figs. 11a and 11b illustrate a 180° phase change (sign inversion) as the signal passes through the signal null of the inversion recovery curve ($M(\tau) = 0$ at $\tau = -T_1 \ln(\frac{1}{2})$). A unitary Fourier transformation subsequently converts the phase cycling dimensions into the respective coherence domains, gathering the majority of the signal into the correct coherence pathway. This indicates that the majority of the equilibrium magnetization goes toward generating the signal of interest – as opposed to a situation where pulse misset or inhomogeneities expend a significant portion of the signal on artefactual pathways. Thus, a quick glance at the DCCT map reveals the relative success or failure of the choice of pulse lengths and inter-pulse delays (*e.g.*, the delay between the initial 180° pulse and the second 90° pulse) without the need for phase correction or for intensive data processing.

As before, the Hermitian symmetry test enables an automated means to find and apply the timing correction. Upon shifting $t = 0$ to the center of the echo, much of the first order phase error (which appears as a horizontal color variation in Fig. 11a) along the x-direction disappears (Fig. 11b). Finally, after alignment (Fig. 11c), the phase cycling noise reduces in intensity.

During the alignment procedure here and in the following results, five features prove to be essential. First, the algorithm must perform any timing (first order phase) corrections before alignment, since signals of different phases do not align properly. Second, a long acquisition (corresponding to a well-resolved, if noisy, frequency domain) capable of capturing sharp features yields the most dramatic improvements. Third, to allow for high resolution in the calculated $\nu_{shift,max}$, a significant zero-filling of the time domain, together with a simple (exponential or Tukey) apodization precedes Fourier transformation to the frequency domain. Fourth, Eq. (23) requires a cross-correlation function for each transient cross-correlated against all others, which permits higher SNR than, *e.g.*, calculating only cross-correlations for nearest-neighbor transients, as might be implied by Eq. (20). Finally, as noted in Sec. II.1.F, optimizing the masked energy/norm of the signal, rather than the full energy/norm of the signal, proves to be essential. Once the echo signal is aligned, the FID is isolated Eq. (3), and its Fourier trans-

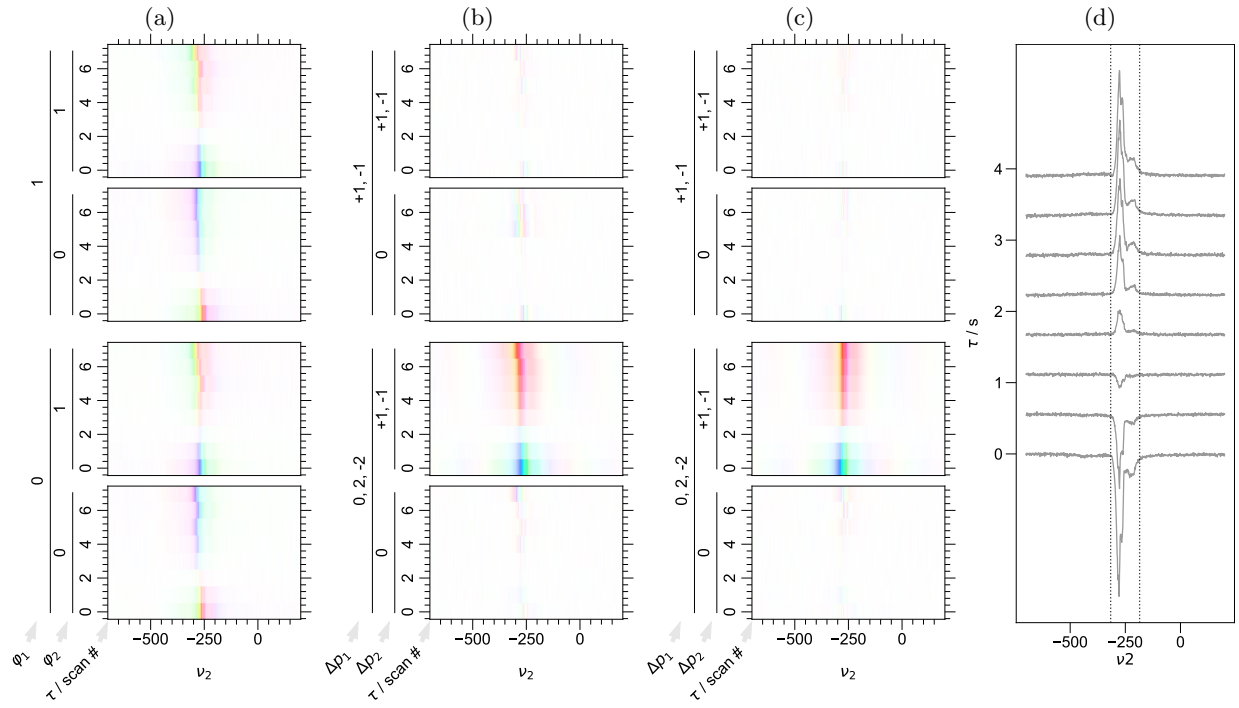

FIG. 11. Application of the processing and visualization algorithms to an inversion recovery experiment produces a high-quality result, despite fluctuating fields and imperfections in phase cycling. In (a), the raw data has not been Fourier transformed along the phase cycling dimension. Here, because the τ values are not equally spaced, the labels on the indirect dimension correspond to the scan number. This data already clearly shows a null followed by phase inversion along the indirect dimension. Fourier transformation of this data from the phase cycling to the coherence domain yields a DCCT map shown in (b), where the Hermitian symmetry cost function Eq. (10) determines the center of the spin echo, yielding phase-corrected signal. The alignment routine corrects the frequency drift, yielding (c). Finally, after slicing out the FID in the time domain, following Eq. (3), (d) provides the real part of the signal, free of baseline distortion, with automatically chosen integration bounds delineated by the dotted lines.

form is shown in Fig. 11d.

IV.4.D. Example: Progressive Enhancement

Following the same data treatment applied to the inversion recovery dataset shown in Fig. 11 and discussed in Sec. IV.4.C, Fig. 12 presents data for a progressive enhancement experiment for an aqueous 6 mM TEMPOL sample. Notable features of this data include an increase in signal intensity along the indirect dimension, p (µw power) as well as an inversion of the data following the first indirect step (corresponding to the point at which ODNP polarization transfer exceeds the thermal polarization). The raw data in the frequency domain shows the characteristic banding expected of an echo detected without a timing correction, in Fig. 12a. The timing correction (Fig. 12b→Fig. 12c) makes the signal phase uniform across all frequencies and coherent (one color) along the indirect dimension. The correlation alignment (Fig. 12c→Fig. 12d) removes the scan-to-scan shifting of the signal and also relieves the slight phase cycling noise, as shown in Fig. 12d. Lastly, the data with integration bounds is shown in Fig. 15a.

IV.4.E. Lineshape Improvement and Choice of Integration Bounds

ODNP and other low-field MR techniques require care when filtering and apodizing the data. Therefore, this section investigates the interplay of the DCCT technique with these methods.

To filter out unwanted frequencies in an experiment, the operator inspects the frequency-domain DCCT map and slices out the portion of the frequency axis containing significant signal, thus filtering out off-resonance noise and reducing the memory footprint of the signal. Domain coloring significantly assists in this process, since incoherent noise appears as a multi-color scatter that can appear grey at a distance, while the weaker shoulders of peaks, *etc.*, trend toward a common color, as exemplified in Fig. 16. The pySpecData library accepts slices given in frequency units (not requiring an array index) in a compact notation (listing A.3) and automatically recalculates the new time axis (since the slicing operation increases the spacing between the time-domain datapoints).

Fig. 13a presents preliminary data from an echo-detected inversion recovery experiment conducted on a sample of 150 µM TEMPOL in toluene; this particular inversion recovery was conducted with no microwave

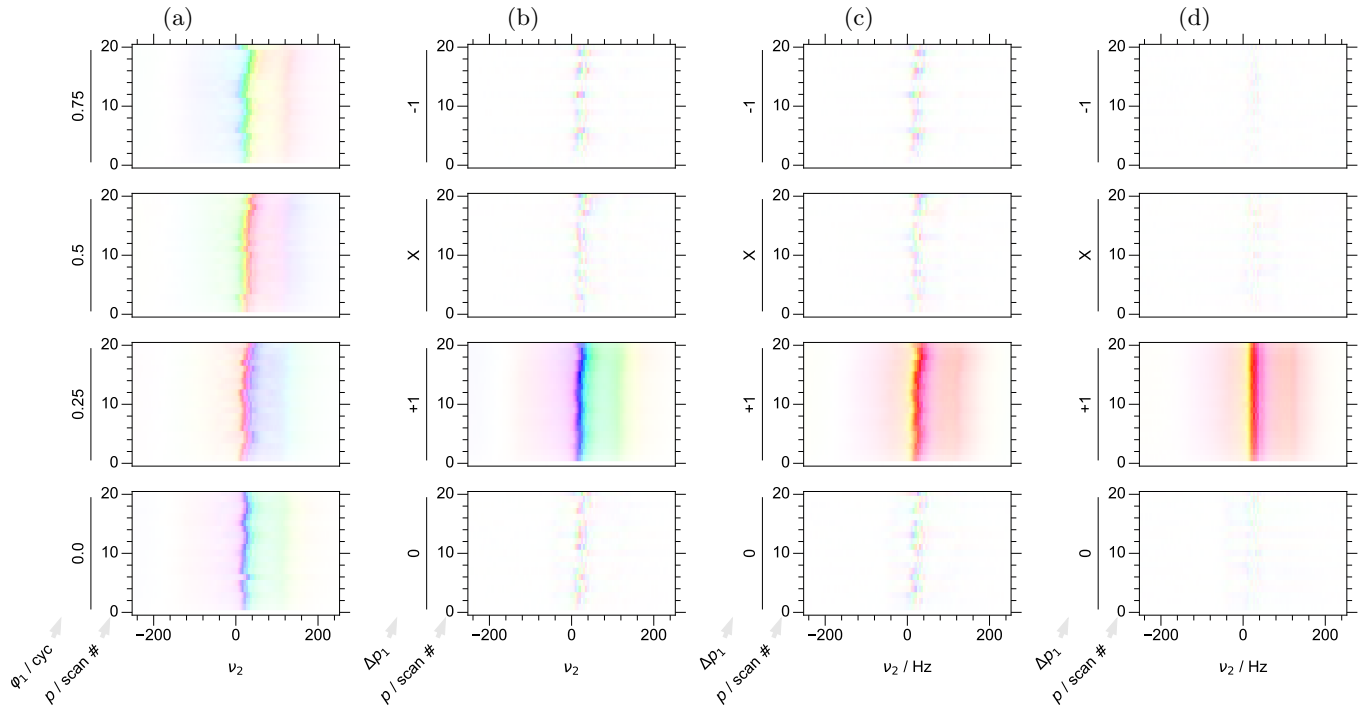

FIG. 12. Similar to Fig. 11 but applied to a progressive enhancement experiment. Here, because the microwave power (p) values are not equally spaced, the labels on the indirect dimension correspond to the scan number. (a): The raw data is Fourier transformed only along the direct dimension; (b): Fourier transformation has been applied along the phase cycling dimension to yield coherence transfer dimension; (c): A timing correction corresponding to $\Delta t_{min}/2$ from Eq. (10) has been applied. (d): The data after applying the correlation alignment. The 1D line plots for this data are shown in Fig. 15a.

power, thus without ODNP signal enhancement. For compactness, it shows only the coherence pathway of interest ($\Delta p_1 = +1$, $\Delta p_2 = -2$). This dataset presents a few challenges: SNR is limited, the acquisition time is relatively short – reflected here as a pixelation along the direct dimension (which has not been zero-filled), and the resonance frequency varies slightly with the magnetic field of the electromagnet. Despite these issues, two distinct peaks (here vertical red bands of color) appear in the correct block of the DCCT map. Furthermore, despite the fact that, the echo time is relatively short, Eq. (12) can determine the center of the echo to enable facile phasing. The peaks in Fig. 13a (blue-green at lower scan number and red at higher scan number) fade off into a constant yellow-green and purple color to either side of the direct frequency dimension. When properly phased, large portions of the dispersive tails of peaks present a constant imaginary phase that does not vary in phase with frequency (because the phase of a Lorentzian follows an arctan function as a function of frequency). Therefore, the yellow-green and purple regions are the dispersive tails of the resonance and the consistency of their coloration indicates that the FID has been correctly sliced from the echo with no further phasing correction required.

Most standard NMR data-processing routines involve filtering in the time domain (apodization), with the specific goal of reducing or eliminating the contribution of noise from points where the signal has decayed to near zero. However, this step requires more care than frequency domain filtering. Inhomogeneities frequently lead to sharp peaks in otherwise broad lineshapes, meaning that signal in the direct time domain does not decay with a single T_2^* time constant. Optimal processing of ODNP data, therefore, requires acquisition with a long direct dimension (corresponding to more detailed frequency resolution) followed by apodization that filters out unnecessary noise. In particular, tests on the results acquired on customized instrumentation (where the acquisition length can sometimes be limited) indicate that proper treatment of the time domain signal is required for attempts at phasing by Eq. (12) or at alignment (as will be discussed later). Specifically, the acquisition length must either exceed $5/\pi\times$ the linewidth of the finest feature or else must be multiplied in the time domain by an exponential decay (*i.e.*, apodized) whose time constant is at most $1/5^{th}$ of the total acquisition length. For example, the proper application of Eq. (12) to generate Fig. 13a requires such apodization. While workarounds based on non-Fourier processing methods [71–75] exist, attempts to ignore this reality using Fourier-based algorithms lead either to issues with peaks described by relatively few points (pixels in the DCCT representation) or with peaks subjected to dramatic sinc interpolation.

Ideally, knowledge of the time-domain decay of the signal envelope guides the choice of a well-matched apodiza-

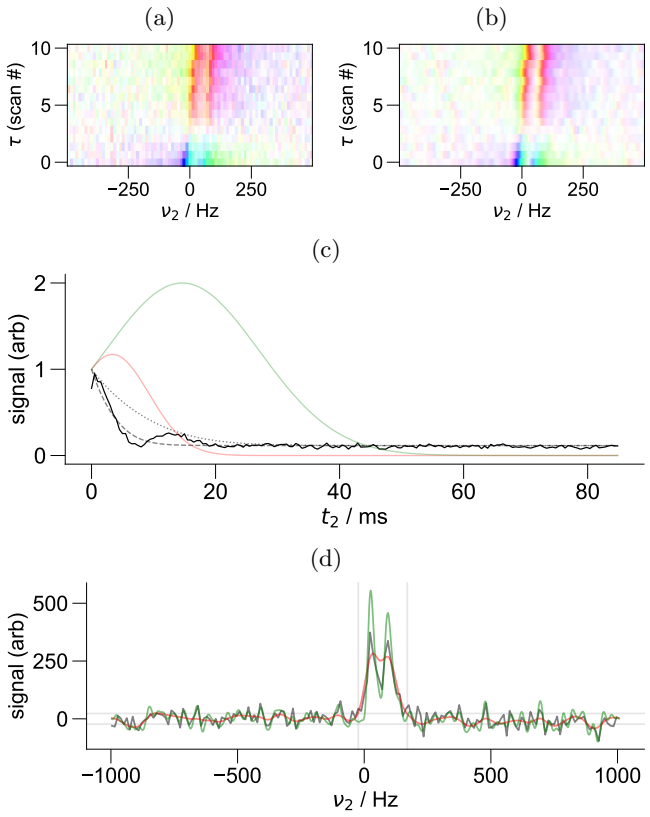

FIG. 13. NMR signal for an inversion recovery dataset of a 4.8 µL toluene sample, showing the subset of the DCCT map (a): before and (b): after equal linewidth L2G apodization, which shows an improvement in resolution with no noticeable change in SNR. (c): The FID signal envelope (solid line) is fit to a model (dashed line) and then expanded to trace the envelope edge (dotted line), along with the resulting apodization functions with equal energy L2G shown in red and equal linewidth L2G shown in green. (d): The real 1D spectra demonstrates the application of filters from (c), where red corresponds again to equal energy and green to equal linewidth, compared against the original 1D spectra in black. The grey horizontal lines superimposed on the spectra indicate the noise levels (from the fit in (c)) and the vertical lines suggest a choice of integration bounds.

tion function. The varying signal phase and frequency in Fig. 13a indicate a preference for finding the signal envelope by summing the absolute value of the individual scans in the time domain. A simple least squares fit of the result to Eqs. (15) and (17), in general, properly determines both the peak amplitude (A) and noise level (σ_n) of the signal. However, the least squares fitting algorithm adjusts the parameters associated with linewidth (λ_L) in a manner inconsistent with tracing the outer edge of the signal envelope – instead passing through the middle of any oscillations. Therefore, keeping the same functional form, the code scans from a minimum λ_L (here, typically 10 Hz) up to the least-squares fit value of λ_L, and determines the norm of the data exceeding the fit function at each linewidth. The point where this norm is a fifth of the way from its lowest value to its highest value (at the least squares λ_L) is chosen as the λ_L of the envelope. The dotted line in Fig. 13c shows the envelope calculated for the toluene data.

Armed with this choice of an enveloped-matched filter (Fig. 13c), the results of Fig. 13 explore the impact of some common apodization functions. Some instances of ODNP benefit from the ability to resolve chemical shifts, as demonstrated recently in several contexts [19, 76]. In Fig. 13b an equal-linewidth L2G transformation (Eq. (19)) aids the resolution of two peaks in the NMR spectrum without noticeably degrading the SNR. Notably, the apodization emphasizes a faint white region between the peaks with neither dispersive/imaginary (yellow-green or purple) nor absorptive/real (red) signal. Fig. 13d demonstrates the same effect in 1D format and also the impact of an equal-energy L2G transformation (Eq. (18)), which slightly degrades resolution, but significantly reduces the noise. It is also interesting to note that (not shown here), by emphasizing particular regions of time, the apodization function can have a notable effect on the inactive pathways in the coherence domain, reducing some phase cycling noise and/or reducing the amplitude of artefacts that occupy different portions of the time domain *vs.* the signal. The equal-energy transformation improves the SNR of the peak, without significantly broadening the range over which it is nonzero. A procedure to automate the choice of integration bounds can apply Eq. (18), and also use the σ_n fit from the envelope equation (Eq. (17) and Fig. 13c) to determine the integration bounds from the points where the (equal energy L2G) apodized peak intersects with 0.5 the standard deviation of the noise of the original spectrum. The grey lines in Fig. 13d provide an example of the procedure for the present data. Overall, the results shown and discussed here emphasize that a well-chosen implementation of the standard technique of L2G apodization provides significant benefit to low-field ODNP data and that these effects contribute cooperatively to the benefits of the DCCT map.

IV.4.F. Example: Integration of Inversion Recovery and Progressive Enhancement

Every rigorous ODNP dynamics analysis following the current standard protocol [15] requires a series of inversion recovery ($R_1(p)$) and progressive enhancement ($E(p)$) measurements and demands a means to easily process the raw data and unambiguously determine the relevant parameters (see Sec. II.2) without significant user input. An important component of this challenge involves converting spectra along the direct dimension (ν_2) into signal intensities. Figs. 14 and 15 compare data that has been integrated, both with and without first implementing the correlation alignment of Sec. IV.4.B and shown in Figs. 11c and 12d.

First, we consider the inversion recovery data. A significant improvement in the signal alignment is observed in Fig. 11c, indicated by the consistent color and intensity of the pixels along the τ axis, which is not observed

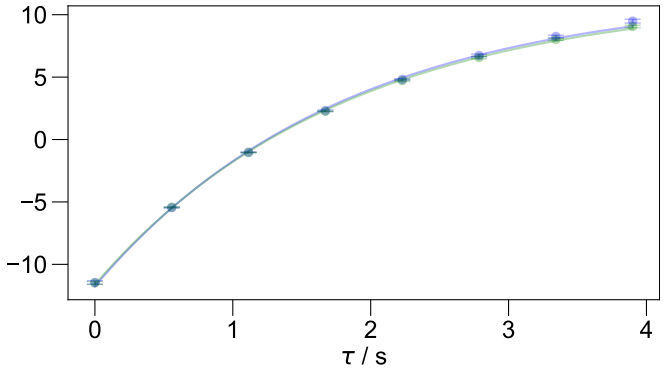

FIG. 14. Integrated inversion recovery signal (with interpulse recovery delay τ) before correlation alignment in blue and after alignment in green. The integrals before and after alignment show essentially no difference, apart from tighter error bounds signifying that the alignment improves experimental error.

in Fig. 11b before alignment. In addition, an inspection of the DCCT map shows much weaker signal intensity in the inactive coherence transfer pathways, corresponding to reduced phase cycling noise. Integrals, of course, prove somewhat forgiving of the resulting errors in the unaligned signal. The expected noise variance of an integral over a given bandwidth can be determined from standard error propagation formulae to be $\sigma_\nu^2 N \Delta\nu^2$, where σ_ν^2 gives the variance of the frequency-domain datapoints, $\Delta\nu$ gives the spacing between them, and N is the number of points. Thus, the errors (standard deviation) scale with the square root of the size of the integration window. Fig. 14 shows modest improvement in the integrals after alignment: tighter integration bounds slightly reduce the error of the aligned signal. In keeping with the smaller error bars, as well as the less ambiguous choice of the integration bounds, alignment also corrects the two datapoints at longer recovery delay with both showing a better fit to the model (Eq. (32)) after alignment.

The signal intensities for progressive enhancement ($E(p)$) data were considered somewhat more carefully. Here, after slicing out the FID from the data of Fig. 12d, the code applies an equal-energy L2G apodization Eq. (18) to improve the SNR of the signal. Because this data comes largely from highly enhanced signal, the result gives a controlled example where the main concerns focus on issues of field stability and misalignment. The stability of the signal is somewhat run-dependent, with the data in Fig. 15a an example of fairly stable progressive enhancement signal. While the lineshape of the aligned signal (green) remains relatively consistent, the lineshape of the unaligned signal (blue) slightly varies – not only in the position of the central peak but also in terms of subtle variations of the shoulder. While the unaligned signal demands integration over fixed bounds, the aligned signal proves amenable to a weighted sum over the lineshape, resulting in tighter error bars (propagated from the noise of the datapoints) that produce a tight

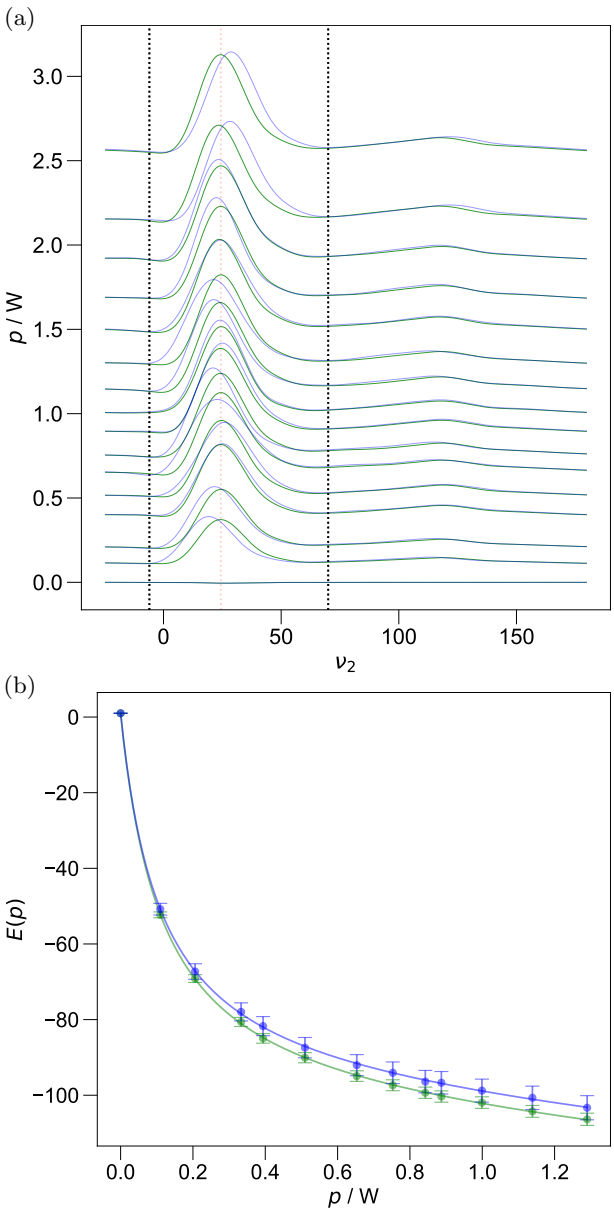

FIG. 15. The NMR signal intensity is determined for a progressive enhancement experiment on 6 mM aqueous TEMPOL (same data as Fig. 12), both without (blue) and with (green) alignment. (a): The real part of the spectrum after slicing out the FID and applying equal-energy L2G apodization with integration limits indicated, before alignement in blue and after alignment in green. The dashed vertical lines provide the integration bounds, while the red line provides a guide to the eye. All signal has been inverted and two scans have been omitted for the sake of presentation clarity, (b): Normalized integral intensities are denoted by circles with accompanying error bars, while the smooth line gives the least squares fit to Eq. (30). Both sets of data were phase corrected. In both cases, error propagation of the noise in inactive coherence channels give the noise of the integrals, which standard error propagation formulas then modify upon normalization. Correlation alignment refines integration bounds, overall improving SNR.

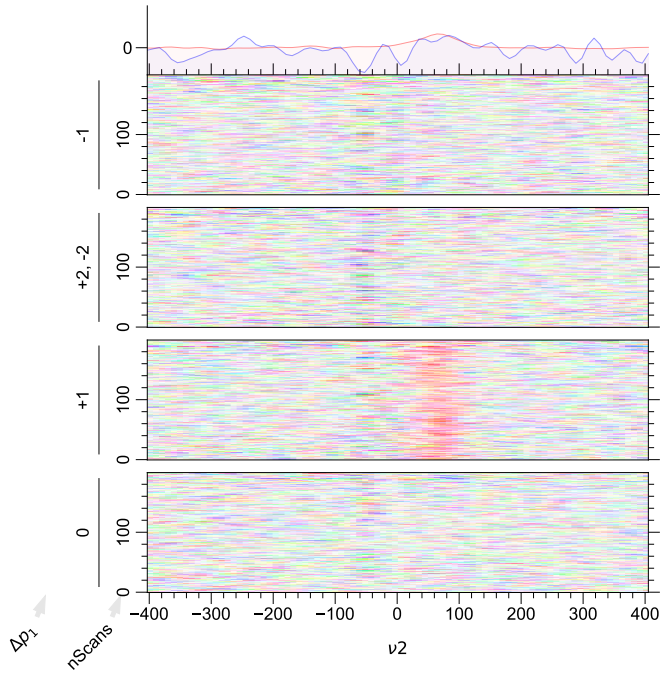

FIG. 16. A portion of the DCCT map for the signal from a reverse micelle sample, before undergoing the correlation alignment. The DCCT map allows the separate display of scans, while also emphasizing the phase-coherent signal. This map only shows the $\Delta p_2 = -2$ portion of the coherence domain for the second pulse, as the other CT pathways include only noise similar to the noise-only pathways that are shown here. The signal appears in red in the expected pathway but is very faint. The 1D plots illustrate that signal is not observable from a single phase cycled scan of the 1600 scans (blue) and is faintly detectable upon averaging over all of the scans (red).

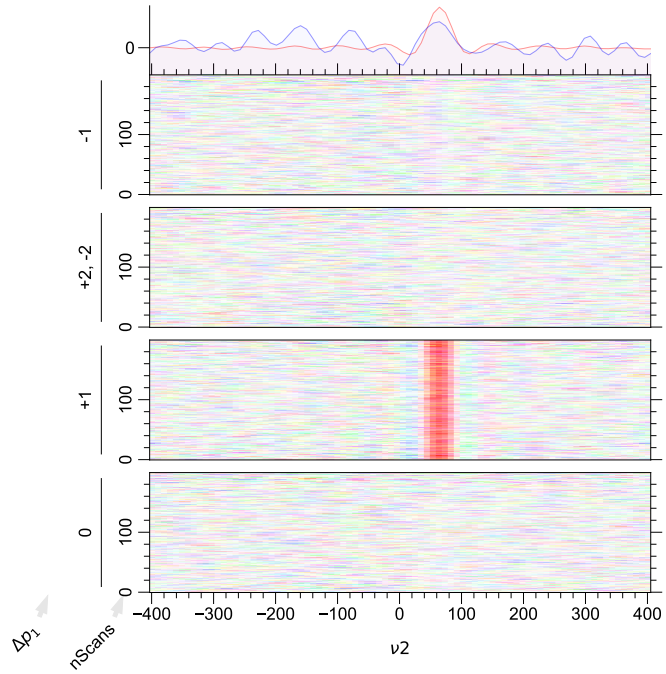

FIG. 17. The same portion of the DCCT map for the data in 16 after undergoing the correlation alignment in Eq. (29). Signal concentrates into a bright red band in the appropriate coherence pathway. The 1D plots illustrate that signal is marginally observable from a single scan out of the 1600 scans (blue); this arises from the alignment of the various transients in the phase cycle. An average taken over all scans significantly improves the signal amplitude (red) and does so with much greater efficiency when the signal has been previously aligned than in the absence of alignment.

match to the model (R^2 0.9987 for unaligned 0.9995 for aligned). The overall scaling of the error bars for the unaligned integration proves very sensitive to the choice of integration bounds (data not shown); however, no such ambiguity exists for the weighted average. This offers promise for not only the precise quantification of important reference standards for ODNP, as done here, but also for a complete ODNP analysis of samples with very low concentrations of either spin label or water.

IV.4.G. Example: Thermal Scan on Reverse Micelles

Typical ODNP studies rely on the fact that water comprises most of the sample, enabling the use of relatively small sample volumes ($\sim$ 4.8 µL). Studying the water inside reverse micelles proves challenging, as the proton spectra present $\sim 1/30\times$ the SNR of aqueous samples. However, with longitudinal relaxation rates, R_1, that are significantly faster (*e.g.* $\sim 7.7\ \mathrm{s}^{-1}$) than those of aqueous solutions ($\sim 0.4\ \mathrm{s}^{-1}$), reverse micelles provide an opportunity for rapid signal averaging not otherwise possible in typical ODNP samples. ODNP studies of solutions of organic solvents typically employ larger sample volumes (even in recent studies [77]), following the rationale that much of the sample is made of low-loss dielectric solvent that can extend into the electric field of the cavity with less substantially detrimental heating effects. However, water and dielectrically active surfactant comprise an uncomfortable intermediate fraction of the sample, resulting in a lower water NMR signal density, but still (based on changes to cavity Q) presenting a significant concern *w.r.t.* sample heating. Thus, even though initial reverse micelle studies used large probes and subsequently larger sample volumes [17], studies of the dynamics of water inside the reverse micelles still require a small (≤ 0.6 mm) sample radius in order to minimize heating effects.

Fig. 16 shows a portion of the DCCT map for thermally polarized spin echo NMR signal for a reverse micelle sample. To compensate for the very low ^{1}H content of this system, the pulse sequence cycles through the 8-step spin echo phase cycle 200 times, resulting in 1600 individual transients. The 1D plots at the top of Fig. 16 show the spectrum from one complete phase cycle (*i.e.* one scan) in blue, as well as the average over all 200 scans in red. While individual transients have insufficient SNR to clearly identify signal, acquiring many transients can lead to broadening of the averaged signal in the presence of slow field drift, rendering characterization of thermal

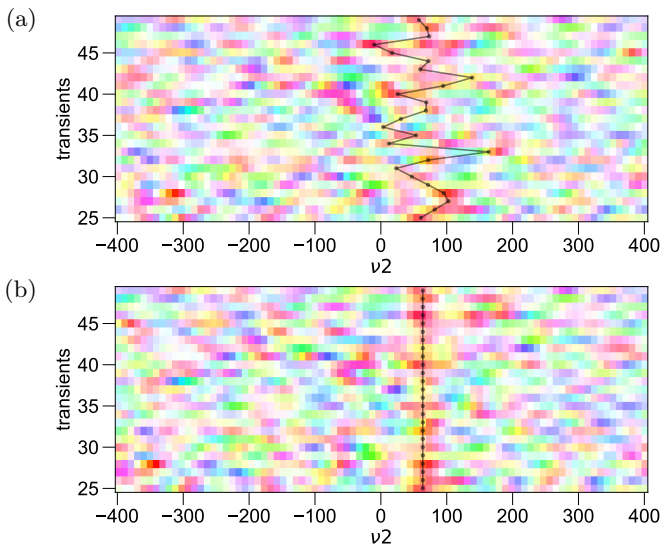

FIG. 18. (a) The DCCT map shows only 50 transients of the coherence channel of interest, for the reverse micelle sample in Sec. IV.4.G before undergoing the correlation alignment. The transients axis represents a direct product of the pulse phase dimensions and the nScans dimension of Figs. 16 and 17. A black line at 50 Hz indicates the expected signal offset. (b) After undergoing the correlation alignment, signal is clearly discernible from noise as a red streak across all scans centered at 50 Hz (indicated by the black line). Note that the alignment routine chooses the center of the signal to be not only typically in-phase red (0°) signal, but also that the signal ~ 40 Hz to the left (smaller frequencies) of the chosen point is more frequently purple or blue ($-60°$ or $-120°$) when compared to frequency with random noise.

signal particularly problematic. In contrast to either of the 1D plots, the DCCT map shows an obvious red band of signal in the expected coherence channel at +75 Hz offset. It also shows that the signal appears to randomly drift over 50-75 Hz throughout the course of the experiment.

Despite the low SNR of the experiment, the signal-averaged correlation function (Eq. (23)) should still be able to align the various transients, since the correlation functions used to determine the frequency shifts are each averaged from 200 separate correlation functions (one for each pair of transients in the experiment). Indeed, after the correlation alignment (Fig. 17), signal again appears in the expected coherence channel, but now as an even more distinct band of a solid color that spans the 200 phase-cycled transients – namely the intense red band at 50 Hz, with blue side bands arising from truncation of the rising portion of the echo. The 1D plot shows that, after the correlation alignment, signal is observed after a single phase cycle (blue), and improved and reduced in noise significantly after averaging over all 200 cycles through the phase cycle (red). This signal exhibits a significantly reduced linewidth of ~ 125 Hz, explained by the alignment of the consecutive transients shown in Fig. 18.

Even though the net signal energy, averaged across repeats, remains the same, aligning the signal improves the phase coherence of the signal from transient to transient. Fig. 16 *vs.* Fig. 17 demonstrates a visual explanation of this process that improves the SNR slightly within each phase cycled scan. A visual effect arising from the improved phase coherence between adjacent scans also likely contributes to the increased visibility of the signal in Fig. 17. Overall, the signal-averaged alignment makes the signal much more visible in not only the averaged signal but also within the individual scans displayed in the DCCT map. This is a striking and somewhat unexpected result.

V. Discussion

The results here advocate for a non-standard approach to utilizing coherence pathways. The DCCT schema comprises 4 interdependent features: (1) storage of all transients (*i.e.*, not phase cycling the receiver and/or averaging on-board), (2) multidimensional organization of data, (3) object-oriented code that assists in data manipulation, and (4) visualization of data as a DCCT map at a relatively early stage of the data processing.

The visualization of all separable coherence pathways along an additional, short dimension, enables efficient diagnosis and mitigation of effects as simple as instrument miscalibration and as subtle as the phase cycling noise caused by unstable fields. In fact, as shown in Sec. IV.3.A, less specialized equipment – *i.e.*, hardware without the capability to phase cycle the receiver – requires this approach in order to separate the desired signal from undesired artefacts.

One notable observation is the fact that domain coloring combines synergistically with the simultaneous presentation of multiple CT pathways. In particular, domain coloring enables the straightforward, simultaneous visualization of all CT pathways by bypassing complexities that arise when different pathways have different phases or timings and/or varying resonance frequencies. By offering a direct, compact visualization of phase coherence as pixels of matching or slowly varying color, the DCCT map also serves as an excellent tool for detecting signals that might otherwise appear to be only noise. In contrast, a lack of coherence, *e.g.*, between echo centers of subsequent scans in the presence of field instabilities (Fig. 6), also becomes quite obvious. Observation of low-SNR DCCT maps motivated the development and implementation of the signal-averaged mean-field correlation alignment presented here, which results in a very clear improvement in the signal linewidth, SNR, and the means for quantifying signal.

While traditional techniques involve discarding at least some data (undesired CT pathways, the imaginary part of data, *etc.*), DCCT maps afford a comprehensive overview of all acquired data in one image, at a very early stage of data processing. Importantly, the DCCT map can yield these results and other informative comparisons

between datasets without first requiring detailed phasing or other manipulation of the raw datasets (Figs. 2, 3 and 5). Thus, the DCCT schema enables deterministic and rapid progress toward acquisition and optimization of NMR signal. The studies here, in particular, demonstrate that DCCT maps prove invaluable in the initial stages of instrument setup, as well as in diagnostic efforts for failed experiments – *e.g.*, the incorporation of new probes or receiver chain components – thus providing significant support for instruments with modular capability. These results also showcase the ability of the DCCT map to highlight three important features of the data: (1) the desired signal in the desired CT pathway, (2) artefacts arising from artefactual pathways and potentially contaminating the desired pathway, and (3) phase cycling noise spread across multiple pathways.

An argument can be made that standard data processing technology frequently lags behind the established understanding of coherence pathways by jumping straight to the selection of the desired coherence pathway. Even though researchers were aware detailed analysis of coherence pathways could enrich experimental design [78], and one could infer similar gains by extending such an analysis to the development of data-processing algorithms, it was frequently necessary to skip the development of such algorithms due to the resulting complexity and incompatibility with standard acquisition techniques and data processing software. As has repeatedly been noted in the literature [26–28, 30, 31], the days before direct detection and digital filtration of rf signals (when limited memory space requirements and slow data transfer rates were a primary concern) have left many historical artefacts that continue to impact typical current approaches to NMR data acquisition and processing. In particular, the rather stringent constraints of minimizing the size of temporarily-stored time domain data through onboard averaging of transients acquired with different phases motivated the design of what has become the traditional methodology for treating coherence pathways in NMR [79]. While the traditional schema still proves optimal in many cases, equipment available today welcomes virtually cost-free storage of all transients in a phase cycle. The DCCT schema outlines a straightforward means to profit from these benefits *via* object-oriented treatment of the resulting multi-dimensional data and robust multi-color domain coloring plots. Importantly, it does not add any time cost to a more traditionally-acquired NMR experiment.

The DCCT approach is not without historical precedent. Very early examples within the context of multiple quantum spectroscopy [25, 29, 58] explicitly Fourier transform along a dimension where phases were cycled in a procedure formalized as the "Phase Fourier Transform." More recently, separate storage of the transients to perform this transformation has proven advantageous in 2D multi-quantum experiments, such as in multiplex phase cycling [26] and MQD [27], as well as in echo train experiments [28]. It is therefore important to note that many modern laboratories utilize a methodology similar to a subset of the DCCT schema, although the authors are unaware of an extant formal description of this very useful procedure in the literature, nor of a consistent and convenient accompanying data-visualization technique, like the one presented here. As observed in the current contribution, the general concept garners the widest utility when also used as a means to explicitly consider signal in regions of the coherence domain that are *not* selected by the pulse sequence.

The DCCT schema, further, offers a means for visually representing several known but important properties of phase cycling. For example, Plancheral's theorem emphasizes that the noise from different transients in the phase cycle domain will spread equally across the coherence domain. Therefore, the selection of a single coherence pathway yields the same SNR benefit as (not phase cycled) signal averaging. The low field experiments in the results here typically benefit from the added SNR of additional phase cycling, since these studies tend to be SNR-limited. However, for the implementation of more elaborate pulse sequences, one desires a straightforward strategy for choosing an optimal phase cycle [78]. The DCCT schema offers such a strategy. Specifically, a DCCT map of signal from a comprehensive phase cycle (*e.g.*, where all pulses are phase cycled by 4 or more steps) would clearly show where in the coherence domain (for which values of Δp_1, Δp_2, *etc.*) artefacts occur and where they do not occur; this clearly indicates which parts of the phase cycle can be reduced and which cannot. Eliminating or reducing the number of phase cycle steps for pulses whose coherence domain shows only noise along one or more dimensions only decreases SNR. In contrast, eliminating or reducing the phase cycle for pulses where the coherence domain shows artefactual signal will alias those artefacts [25], potentially into the desired coherence pathway.

As a simple example, in Fig. 5, elimination of the phase cycle of the first pulse would add noise of the $\Delta p_1 = \pm 1$, $\Delta p_2 = \pm 1$ pathway to that of the $\Delta p_1 = 0$, $\Delta p_2 = -1$ pathway and the noise of the $\Delta p_1 = 0$, $\Delta p_2 = 0$ pathway to the $\Delta p_1 = +1$, $\Delta p_2 = -2$ pathway. While this decreases the SNR by $\sqrt{2}$, the artefact ($\Delta p_1 = 0$, $\Delta p_2 = -1$) remains separated (no significant DC artefacts at $\Delta p_1 = 0$, $\Delta p_2 = 0$ are present here), and the number of scans reduces by a factor of 2. In contrast, elimination of the phase cycle altogether adds all four coherence pathways together, superimposing the FID-like artefact in $\Delta p_1 = 0$, $\Delta p_2 = -1$ onto the actual echo signal in $\Delta p_1 = +1$, $\Delta p_2 = -2$. Similarly, the CPMG results in Fig. 7a indicate when a 4-step *vs.* 2-step phase cycle of the excitation pulse proves useful. These are simple examples, but provide a demonstration of an empirical method that can be extended to more complex pulse sequences.

For application to experiments in electromagnets and other non-ideal fields, the results here advocate a strategy of acquisition lengths spanning many times the T_2^* (with

ideal timescales governed rather by the sharpest features of the lineshape), with phasing identified from the Hermitian symmetry of the echo signal (Sec. II.1.D), followed by alignment (Sec. II.1.F) and apodization (Sec. II.1.E). The benefits of echo-based detection complement the DCCT schema, as echo-based signal follows a distinctive coherence pathway. Thus, phase cycled echoes offer particular advantages over 90° pulse-acquire schemes when acquiring signal on a system for the first time. Aside from offering a maximum signal intensity that is not sensitive to field inhomogeneity, echo signals are also cleanly isolated from any ringdown arising from the pulses. The signal appears in 1 out of the 8 separate pathways in the coherence domain that are resolved by a typical phase cycle, and it can be compared to the amplitude of the noise and artefacts of signal in these other pathways. Furthermore, echo-based signals do not require post-processing (*e.g.*, linear prediction or polynomial fitting) to yield baseline-free spectra, which here proves ideal for the quantitative NMR necessary for ODNP.

Beyond these specifics, however, the most important overarching result reported here is the unexpected synergy between domain coloring for the visualization of signal phase, the simultaneous visualization of all coherence pathways, and modern object-oriented programming that enables organization and plotting of the data.

VI. Conclusion

The DCCT schema offers a powerful new standard for visualizing data (the DCCT map) that proves unexpectedly useful and versatile. The results presented here highlight the DCCT schema as critical for quickly identifying and optimizing signal in the presence of obstacles such as inhomogeneous fields or reduced SNR, as in low field NMR. As repeatedly noted in the literature, eschewing on-board signal averaging offers a range of practical benefits, but beyond this the DCCT schema provides a detailed yet comprehensible view of all of the data acquired during the course of an NMR experiment, leading to a significant degree of confidence in the quality of the results and subsequent data processing. This technique also serves as a means to elucidate experimental errors that otherwise would be overlooked, serving to improve the overall execution of NMR. Further, the use of the DCCT map to visualize the complete suite of coherence transfer pathways attainable for a given pulse sequence offers insight into empirical phase cycle optimization for a given experiment. The success of these methods in improving the practicability of the modular ODNP system here indicates future successes in other fields of customized NMR. Due to these benefits, the DCCT map will serve as an excellent tool for detecting signal whether in routine spectroscopy of biomolecules, in a spectrometer subjected to appreciable field drift, or in samples with challenging low proton concentrations that would otherwise produce only noise. The ability of the DCCT map to aid in detecting signal despite significant noise has applications to low field systems as well as when dealing with simple but costly human errors on well-configured high field systems. Lastly, the DCCT map is expected to contribute to aid in the development of data processing routines and algorithms, such as the signal-averaged mean-field correlation alignment presented here, given its ability to highlight shortcomings in the execution of NMR experiments. The authors forsee particular applications to pulsed ESR [80, 81] and 2D NMR at low field. However, the target of future applications ranges broadly, from experiments as closely related as portable MR to those as distantly related as two-dimensional coherent laser spectroscopy.

Acknowledgments

This material is based in part upon work supported by the National Science Foundation under Grant No. 2146270. This work is also supported in part by the Syracuse University College of Arts + Sciences in the form of by startup funds, as well as the Graduate School Summer Dissertation Fellowship received by AAB. The authors would like to thank all the members of ACERT and Prof. Jack Freed's lab, as well as members of Prof. Songi Han's lab for fruitful discussions and the opportunity to develop nascent stages of the concepts presented here. The authors would also like to thank the ODNP team at Bridge12 and Dr. Tom Casey for fruitful discussions and to note that several features of the pySpecData library have also been ported to the DNPLab Python package http://dnplab.net/ for broader dissemination to the community.

Author Declarations

The authors have no conflicts to disclose.

Data Availability

Raw datasets underlying all figures are stored in HDF5 format and are freely available from the authors upon request.

A. Code Snippets

The FID is sliced from the echo by subtracting the delay between the start of acquisition and the center of the echo, t_{delay} from the original t_2 axis coordinates, then placing the axis in register (so that one of the axis coordinates occurs at exactly $t_2 = 0$), slicing out only values $t_2 > 0$, and finally setting the first datapoint to 1/2 its original value.

Listing A.1. FID slice

```
s["t2"] -= t_delay # set back the t2 axis
                   # by time t_delay
s.register_axis({"t2":0}) # ensure that the t2
#                           axis contains a
#                           time point 0
s=s["t2":(0, None)] # discard time points
#                     before t=0
s["t2",0] *= 0.5 # multiply first point by 0.5
```

Pulse programs supplied from Bruker implement the 'traditional' schema for phase cycling–namely, cycling of the receiver phase and signal averaging on board.

In order to store all the phase cycled transients separately, slight modifications to existing pulse programs are needed. The following demonstrates a template that has been successfully used to accomplish this task in a Bruker pulse program:

Listing A.2. Separately saved phase cycling in Bruker pulse program

```
"l21=4" ; length of phase program ph1
"l22=2" ; length of phase program ph2
loopcounter num_ph
"num_ph = l21*l22"
; td1 set to total number of transients
; (including the phase cycle)
"l20 = td1/num_ph" ; calculates indirect
                   ; dimension, if it exists
"nbl = num_ph"

1      st0 ; reset buffer pointer to 0 when
           ; phase cycle is complete
2      p1 ph1 ; apply 90 pulse according
              ; to phase program ph1
       ; (rudimentary template showing only key
       ; features -- delays, etc are omitted.
       ; A standard spin echo would have a
       ; delay here.)
       p2 ph2 ; apply 180 pulse according
              ; to phase program ph2
       goscnp ph31 ;acquisition of data,
                   ;rx phase always 0
       st
       ipp1 ; increment phase of first pulse
       lo to 2 times l21 ; controls loop over
                         ; phase program ph1.
                         ; By convention, we
                         ; use loop counter
                         ; 12X for phase
                         ; cycle X
       ipp2 ; increment phase pointer
            ; to program ph2, as outermost
            ; phase cycling loop
    lo to 2 times l22
  wr #0 if #0 id0 ; even for experiments that
  ; don't require d0, id0 is required for
  ; standard behavior
lo to 1 times l20 ; if indirect dimension
                  ; employed, this loop
                  ; generates the indirect
                  ; dimension

; phase programs
ph1 = 0 1 2 3
ph2 = 0 2
ph31=0 ; receiver phase, always 0
;note through loops and phase pointers,
;we avoid:
;ph1 = 0 1 2 3 0 1 2 3
;ph2 = 0 0 0 0 2 2 2 2
```

The following demonstrates the ease with which one can filter along a given axis (here, frequency filtering) in pyspecdata, referring to values along the axis itself, and returning data along that slice.

Listing A.3. Frequency slicing

```
s.ft("t2", shift=True) # Fourier Transform
#                        (shifted to center
#                        about 0 Hz) from the
#                        time to frequency
#                        domain along the
#                        direct dimension.
s = s["t2":(-400, 400)] # slice out the signal
#                         within ±400 Hz of
#                         the carrier
```

The following pySpecData python easily sets the time axis of the data to center the echo at $t = 0$. The data instance `s` is either directly supplied by the spectrometer (utilizing an in-house library for running the SpinCore transceiver) or by loading the relevant Bruker data into pySpecData. Here, we assume that `s` was previously moved from the direct time to frequency domain (*e.g.*, in order to slice out a relevant range of spectral frequencies):

Listing A.4. Setting time axis

```
s.ift("t2")  # move to the time domain
echo_center = hermitian_function_test(
    s
)  # runs the Hermitian function test and
#    returns the center of the echo
s.setaxis(
    "t2", lambda x: x - echo_center
).register_axis(
    {"t2": 0}
)  # applies this best shift to the time axis
```

Acquisition with the digital oscilloscope requires digital demodulation and filtering, which typically takes the following form. (Note how the time domain name for the axis is typically used to refer to the axis, regardless of whether it is currently in the time or frequency domain.)

Listing A.5. Oscilloscope-based acquisition

```
with GDS_scope() as g:
    pulse = g.acquire_waveform(
        ch=1
    )  # typically, split off and capture the
    #    pulse waveform for reference
    s = g.acquire_waveform(
        ch=2
    )  # signal after duplexer and LNA
    pulse.ft(
        "t", shift=True
    )  # move the pulse waveform into the
    #    frequency domain
    center_frq = abs(
            pulse["t":(0, None)]
            ).argmax("t")  # estimate the
    #                        carrier frequency
    #                        from the max
    s.ft(
        "t", shift=True
    )  # move the signal into the time domain
    s = s[
        "t" : (center_frq + r_[-10e3, 10e3])
    ]  # filter out a 20 kHz bandwidth
    s.ift("t")  # move s back to the time
    #             domain
```

Storing each phase cycled transient separately results, in the simplest case scenario, in one long concatenated sequence of complex data (1-dimensional array). One can easily reshape this long 1-dimensional array into the

appropriate dimensions of choice, an operating referred to in pySpecData as 'chunk'-ing.

Listing A.6. Example of chunking data for DCCT

```
s.chunk(
    "t", ["ph2", "ph1", "t2"], [2, 4, -1]
)  # here we break data into phase cycle
#    steps → assuming that the leftmost
#    dimension is iterated by the outermost
#    loop of the pulse sequence while the
#    rightmost label is iterated by the
#    innermost loop of the pulse sequence
#    (typically the counter for the direct
#    acquisition datapoints)
s.setaxis(
    "ph1", r_[0:4] / 4
)  # label the phase cycling dimension, in
#    units of cycles -- the first pulse here
#    is cycled in 4 steps
s.setaxis(
    "ph2", r_[0:2] / 4
)  # label the phase cycling dimension, in
#    units of cycles -- the second pulse here
#    is cycled in 2 steps
s.ft(
    ["ph1", "ph2"], unitary=True
)  # Fourier Transform to move from the phase
#    cycling domain to the coherence domain →
#    this example employs a vector-unitary
#    Fourier Transformation (which preserves
#    the vector norm)
s.ft(
    "t2", shift=True
)  # Fourier Transformation from the time to
#    frequency domain along the direct
#    dimension
DCCT(
    s["t2":(-500, 500)]
)  # generate a DCCT plot over the
#    range ±500 Hz
```


[1] B. D. Armstrong and S. Han. "Overhauser dynamic nuclear polarization to study local water dynamics." *J. Am. Chem. Soc.*, 131(13):4641–7 (2009). PMID: 19290661. doi:10.1021/ja809259q.

[2] J. M. Franck, A. Pavlova, J. A. Scott, and S. Han. "Quantitative cw Overhauser effect dynamic nuclear polarization for the analysis of local water dynamics." *Prog. Nucl. Magn. Reson. Spectrosc.*, 74:33–56 (2013). PMID: 24083461. doi:10.1016/j.pnmrs.2013.06.001.

[3] A. Doll, E. Bordignon, B. Joseph, R. Tschaggelar, and G. Jeschke. "Liquid state DNP for water accessibility measurements on spin-labeled membrane proteins at physiological temperatures." *J. Magn. Reson.*, 222:34–43 (2012). doi:10.1016/j.jmr.2012.06.003.

[4] T. F. Segawa, M. Doppelbauer, L. Garbuio, A. Doll, Y. O. Polyhach, and G. Jeschke. "Water accessibility in a membrane-inserting peptide comparing Overhauser DNP and pulse EPR methods." *J. Chem. Phys.*, 144(19):194201 (2016). doi:10.1063/1.4948988.

[5] T. Überrück, O. Neudert, K.-D. Kreuer, B. Blümich, J. Granwehr, S. Stapf, and S. Han. "Effect of nitroxide spin probes on the transport properties of Nafion membranes." *Phys. Chem. Chem. Phys.*, 20(41):26660–26674 (2018). doi:10.1039/C8CP04607G.

[6] J. H. Ortony, C.-Y. Cheng, J. M. Franck, R. Kausik, A. Pavlova, J. Hunt, and S. Han. "Probing the hydration water diffusion of macromolecular surfaces and interfaces." *New J. Phys.*, 13(1):015006 (2011). doi:10.1088/1367-2630/13/1/015006.

[7] B. D. Armstrong, M. D. Lingwood, E. R. McCarney, E. R. Brown, P. Blümler, and S. Han. "Portable X-band system for solution state dynamic nuclear polarization." *J. Magn. Reson.*, 191(2):273–81 (2008). PMID: 18226943. doi:10.1016/j.jmr.2008.01.004.

[8] J. M. Franck, R. Kausik, and S. Han. "Overhauser dynamic nuclear polarization-enhanced NMR relaxometry." *Microporous Mesoporous Mater.*, 178:113–118 (2013). PMID: 23837010. doi:10.1016/j.micromeso.2013.04.019.

[9] O. Neudert, D. G. Zverev, C. Bauer, P. Blümler, H. W. Spiess, D. Hinderberger, and K. Münnemann. "Overhauser DNP and EPR in a Mobile Setup: Influence of Magnetic Field Inhomogeneity." *Appl. Magn. Reson.*, 43(1-2):149–165 (2012). doi:10.1007/s00723-012-0347-4.

[10] T. Überrück, M. Adams, J. Granwehr, and B. Blümich. "A compact X-Band ODNP spectrometer towards hyperpolarized 1H spectroscopy." *J. Magn. Reson.*, 314:106724 (2020). doi:10.1016/j.jmr.2020.106724.

[11] V. Denysenkov and T. Prisner. "Liquid state Dynamic Nuclear Polarization probe with Fabry–Perot resonator at 9.2T." *J. Magn. Reson.*, 217:1–5 (2012). doi:10.1016/j.jmr.2012.01.014.

[12] P. Neugebauer, J. G. Krummenacker, V. P. Denysenkov, C. Helmling, C. Luchinat, G. Parigi, and T. F. Prisner. "High-field liquid state NMR hyperpolarization: a combined DNP/NMRD approach." *Phys. Chem. Chem. Phys.*, 16(35):18781–18787 (2014). doi:10.1039/C4CP02451F.

[13] D. Sezer, M. J. Prandolini, and T. F. Prisner. "Dynamic nuclear polarization coupling factors calculated from molecular dynamics simulations of a nitroxide radical in water." *Phys. Chem. Chem. Phys.*, 11(31):6626–37 (2009). PMID: 19639137. doi:10.1039/b905709a.

[14] M. G. Concilio, M. Soundararajan, L. Frydman, and I. Kuprov. "High-field solution state DNP using cross-correlations." *J. Magn. Reson.*, 326:106940 (2021). doi:10.1016/j.jmr.2021.106940.

[15] J. M. Franck and S. Han. "Overhauser Dynamic Nuclear Polarization for the Study of Hydration Dynamics, Explained." In A. J. Wand, editor, "Biological NMR Part B," volume 615 of *Methods in Enzymology*, pages 131–175. Academic Press (2019).

[16] A. Krahn, P. Lottmann, T. Marquardsen, A. Tavernier, M.-T. Türke, M. Reese, A. Leonov, M. Bennati, P. Hoefer, F. Engelke, and C. Griesinger. "Shuttle DNP spectrometer with a two-center magnet." *Phys. Chem. Chem. Phys.*, 12(22):5830–5840 (2010). doi:10.1039/C003381B.

[17] K. G. Valentine, G. Mathies, S. Bédard, N. V. Nucci, I. Dodevski, M. A. Stetz, T. V. Can, R. G. Griffin, and A. J. Wand. "Reverse Micelles As a Platform for Dynamic Nuclear Polarization in Solution NMR of Pro-

teins." *J. Am. Chem. Soc.*, 136(7):2800–2807 (2014). doi: 10.1021/ja4107176.

[18] A. Dey and A. Banerjee. "Unusual Overhauser Dynamic Nuclear Polarization Behavior of Fluorinated Alcohols at Room Temperature." *J. Phys. Chem. B*, page acs.jpcb.9b08144 (2019). doi:10.1021/acs.jpcb.9b08144.

[19] T. J. Keller, A. J. Laut, J. Sirigiri, and T. Maly. "High-resolution Overhauser dynamic nuclear polarization enhanced proton NMR spectroscopy at low magnetic fields." *J. Magn. Reson.*, 313:106719 (2020). doi: 10.1016/j.jmr.2020.106719.

[20] E. O. Stejskal and J. Schaefer. "Comparisons of quadrature and single-phase fourier transform NMR." *J. Magn. Reson.*, 14(2):160–169 (1974). doi:10.1016/0022-2364(74)90270-4.

[21] E. O. Stejskal and J. Schaefer. "Data routing in quadrature FT NMR." *J. Magn. Reson.*, 13(2):249–251 (1974). doi:10.1016/0022-2364(74)90014-6.

[22] D. I. Hoult and R. E. Richards. "Critical factors in the design of sensitive high resolution nuclear magnetic resonance spectrometers." *Proceedings of the Royal Society of London. A. Mathematical and Physical Sciences*, 344(1638):311–340 (1975). doi:10.1098/rspa.1975.0104.

[23] G. Bodenhausen, R. Freeman, and D. L. Turner. "Suppression of artifacts in two-dimensional J spectroscopy." *J. Magn. Reson.*, 27(3):511–514 (1977). doi: 10.1016/0022-2364(77)90016-6.

[24] A. D. Bain. "Coherence levels and coherence pathways in NMR. A simple way to design phase cycling procedures." *J. Magn. Reson.*, 56(3):418–427 (1984). doi: 10.1016/0022-2364(84)90305-6.

[25] G. Bodenhausen, H. Kogler, and R. R. Ernst. "Selection of coherence-transfer pathways in NMR pulse experiments." *J. Magn. Reson.*, 58(3):370–388 (1984). doi: 10.1016/0022-2364(84)90142-2.

[26] N. Ivchenko, C. E. Hughes, and M. H. Levitt. "Multiplex phase cycling." *J. Magn. Reson.*, 160(1):52–58 (2003). doi:10.1016/S1090-7807(02)00108-8.

[27] J. Schlagnitweit, M. Horničáková, G. Zuckerstätter, and N. Müller. "MQD—Multiplex-Quadrature Detection in Multi-Dimensional NMR." *ChemPhysChem*, 13(1):342–346 (2012). doi:10.1002/cphc.201100525.

[28] J. H. Baltisberger, B. J. Walder, E. G. Keeler, D. C. Kaseman, K. J. Sanders, and P. J. Grandinetti. "Communication: Phase incremented echo train acquisition in NMR spectroscopy." *J. Chem. Phys.*, 136(21):211104 (2012). doi:10.1063/1.4728105.

[29] A. Wokaun and R. R. Ernst. "Selective detection of multiple quantum transitions in NMR by two-dimensional spectroscopy." *Chem. Phys. Lett.*, 52(3):407–412 (1977). doi:10.1016/0009-2614(77)80476-4.

[30] Z. Gan and H.-T. Kwak. "Enhancing MQMAS sensitivity using signals from multiple coherence transfer pathways." *J. Magn. Reson.*, 168(2):346–351 (2004). doi: 10.1016/j.jmr.2004.03.021.

[31] C. A. Waudby, M. Ouvry, B. Davis, and J. Christodoulou. "Two-dimensional NMR lineshape analysis of single, multiple, zero and double quantum correlation experiments." *J. Biomol. NMR*, 74(1):95–109 (2020). doi:10.1007/s10858-019-00297-7.

[32] Y.-Y. Lin, S. Ahn, N. Murali, W. Brey, C. R. Bowers, and W. S. Warren. "High-Resolution, $>1\mathrm{GHz}$ NMR in Unstable Magnetic Fields." *Phys. Rev. Lett.*, 85(17):3732–3735 (2000). doi: 10.1103/PhysRevLett.85.3732.

[33] M. G. Raymer, A. H. Marcus, J. R. Widom, and D. L. P. Vitullo. "Entangled photon-pair two-dimensional fluorescence spectroscopy (EPP-2DFS)." *The journal of physical chemistry. B*, 117(49):15559–75 (2013). PMID: 24047447. doi:10.1021/jp405829n.

[34] S.-H. Shim, D. B. Strasfeld, E. C. Fulmer, and M. T. Zanni. "Femtosecond pulse shaping directly in the mid-IR using acousto-optic modulation." *Opt. Lett.*, 31(6):838 (2006). doi:10.1364/OL.31.000838.

[35] J. C. Dean and G. D. Scholes. "Coherence Spectroscopy in the Condensed Phase: Insights into Molecular Structure, Environment, and Interactions." *Acc. Chem. Res.*, 50(11):2746–2755 (2017). doi: 10.1021/acs.accounts.7b00369.

[36] R. R. Ernst, G. Bodenhausen, and A. Wokaun. *Principles of Nuclear Magnetic Resonance in One and Two Dimensions*. Clarendon Press (1987). ISBN 978-0-19-855629-9. Google-Books-ID: XndTnwEACAAJ.

[37] M. Rance and R. A. Byrd. "Obtaining high-fidelity spin-12 powder spectra in anisotropic media: Phase-cycled Hahn echo spectroscopy." *J. Magn. Reson.*, 52(2):221–240 (1983). doi:10.1016/0022-2364(83)90190-7.

[38] P. Callaghan. *Principles of Nuclear Magnetic Resonance Microscopy*. Clarendon Press, Oxford, revised ed. edition edition (1994). ISBN 978-0-19-853997-1.

[39] A. Bax, M. Ikura, L. E. Kay, and G. Zhu. "Removal of F1 baseline distortion and optimization of folding in multidimensional NMR spectra." *J. Magn. Reson.*, 91(1):174–178 (1991). doi:10.1016/0022-2364(91)90422-P.

[40] G. Zhu, D. A. Torchia, and A. Bax. "Discrete Fourier Transformation of NMR Signals. The Relationship between Sampling Delay Time and Spectral Baseline." *J. Magn. Reson. A*, 105(2):219–222 (1993). doi: 10.1006/jmra.1993.1274.

[41] A. Bax and D. Marion. "Improved resolution and sensitivity in 1H-detected heteronuclear multiple-bond correlation spectroscopy." *J. Magn. Reson.*, 78(1):186–191 (1988). doi:10.1016/0022-2364(88)90172-2.

[42] R. P. Futrelle and D. J. McGinty. "Calculation of spectra and correlation functions from molecular dynamics data using the fast Fourier transform." *Chem. Phys. Lett.*, 12(2):285–287 (1971). doi:10.1016/0009-2614(71)85065-0.

[43] H. de Brouwer. "Evaluation of algorithms for automated phase correction of NMR spectra." *J. Magn. Reson.*, 201(2):230–238 (2009). doi:10.1016/j.jmr.2009.09.017.

[44] F. C. Leone, L. S. Nelson, and R. B. Nottingham. "The Folded Normal Distribution." *Technometrics*, 3(4):543–550 (1961). doi:10.1080/00401706.1961.10489974.

[45] S. B. Kim, Z. Wang, and B. Hiremath. "A Bayesian approach for the alignment of high-resolution NMR spectra." *Annals of Operations Research*, 174(1):19–32 (2010). doi:10.1007/s10479-008-0332-3.

[46] D. Ha, J. Paulsen, N. Sun, Y.-Q. Song, and D. Ham. "Scalable NMR spectroscopy with semiconductor chips." *Proc. Natl. Acad. Sci. U.S.A.*, 111(33):11955–11960 (2014). PMID: 25092330. doi:10.1073/pnas.1402015111.

[47] K. A. Veselkov, J. C. Lindon, T. M. D. Ebbels, D. Crockford, V. V. Volynkin, E. Holmes, D. B. Davies, and J. K. Nicholson. "Recursive Segment-Wise Peak Alignment of Biological ^{1} H NMR Spectra for Improved Metabolic Biomarker Recovery." *Anal. Chem.*, 81(1):56–66 (2009). doi:10.1021/ac8011544.

[48] F. Savorani, G. Tomasi, and S. B. Engelsen. "icoshift: A versatile tool for the rapid alignment of 1D NMR spectra." *J. Magn. Reson.*, 202(2):190–202 (2010). doi: 10.1016/j.jmr.2009.11.012.

[49] J. M. Franck, J. A. Scott, and S. Han. "Nonlinear Scaling of Surface Water Diffusion with Bulk Water Viscosity of Crowded Solutions." *J. Am. Chem. Soc.*, 135(11):4175–4178 (2013). doi:10.1021/ja3112912.

[50] G. H. Weiss, R. K. Guptaj, J. A. Ferretti, and E. D. Becker. "The choice of optimal parameters for measurement of spin-lattice relaxation times. I. Mathematical formulation." *J. Magn. Reson.*, 37(3):369–379 (1980). doi: 10.1016/0022-2364(80)90044-X.

[51] S. Hoyer and J. Hamman. "xarray: N-D labeled arrays and datasets in Python." *Journal of Open Research Software*, 5(1) (2017). doi:10.5334/jors.148.

[52] K. Poelke and K. Polthier. "Domain Coloring of Complex Functions: An Implementation-Oriented Introduction." *IEEE Comput. Graph. Appl.*, 32(5):90–97 (2012). doi:10.1109/MCG.2012.100.

[53] D. Foster, C. Kind, P. J. Ackerman, J. S. B. Tai, M. R. Dennis, and I. I. Smalyukh. "Two-dimensional skyrmion bags in liquid crystals and ferromagnets." (2019).

[54] X. Yu, M. Mostovoy, Y. Tokunaga, W. Zhang, K. Kimoto, Y. Matsui, Y. Kaneko, N. Nagaosa, and Y. Tokura. "Magnetic stripes and skyrmions with helicity reversals." *Proc. Natl. Acad. Sci. U.S.A.*, 109(23):8856–8860 (2012). doi:10.1073/pnas.1118496109.

[55] C. A. Meriles, D. Sakellariou, and A. Pines. "Broadband phase modulation by adiabatic pulses." *J. Magn. Reson.*, 164(1):177–181 (2003). doi:10.1016/S1090-7807(03)00157-5.

[56] J. M. Franck, V. Demas, R. W. Martin, L.-S. Bouchard, and A. Pines. "Shimmed matching pulses: Simultaneous control of rf and static gradients for inhomogeneity correction." *J. Chem. Phys.*, 131(23):234506 (2009). PMID: 20025334. doi:10.1063/1.3243850.

[57] J. D. Hunter. "Matplotlib: A 2d graphics environment." *Computing in Science & Engineering*, 9(3):90–95 (2007). doi:10.1109/MCSE.2007.55.

[58] G. Drobny, A. Pines, S. Sinton, D. P. Weitekamp, and D. Wemmer. "Fourier transform multiple quantum nuclear magnetic resonance." *Faraday Symp. Chem. Soc.*, 13:49 (1978). doi:10.1039/fs9781300049.

[59] C. R. Harris, K. J. Millman, S. J. van der Walt, R. Gommers, P. Virtanen, D. Cournapeau, E. Wieser, J. Taylor, S. Berg, N. J. Smith, R. Kern, M. Picus, S. Hoyer, M. H. van Kerkwijk, M. Brett, A. Haldane, J. F. del Río, M. Wiebe, P. Peterson, P. Gérard-Marchant, K. Sheppard, T. Reddy, W. Weckesser, H. Abbasi, C. Gohlke, and T. E. Oliphant. "Array programming with NumPy." *Nature*, 585(7825):357–362 (2020). doi:10.1038/s41586-020-2649-2.

[60] J. Franck, A. Beaton, and A. Guinness. "pyspecdata." http://github.com/jmfrancklab/pyspecdata/ (2016).

[61] Y. Hibino, K. Sugahara, Y. Muro, H. Tanaka, T. Sato, and Y. Kondo. "Simple and low-cost tabletop NMR system for chemical-shift-resolution spectra measurements." *J. Magn. Reson.*, 294:128–132 (2018). doi: 10.1016/j.jmr.2018.07.003.

[62] K. Chonlathep, T. Sakamoto, K. Sugahara, and Y. Kondo. "A simple and low-cost permanent magnet system for NMR." *J. Magn. Reson.*, 275:114–119 (2017). doi:10.1016/j.jmr.2016.12.010.

[63] Note that the ordering of the dimensions in the × expression and in the function are meaningful with respect to the code and imply the ordering of the data dimensions following a "C-type" (as opposed to "Fortran-type") convention, such that datapoints with adjacent indices along the right/inner most dimension reside in adjacent memory locations, while adjacent values in the left/outermost dimension reside further apart in memory.

[64] M. H. Levitt. "The Signs of Frequencies and Phases in NMR." *J. Magn. Reson.*, 126(2):164–182 (1997). doi: 10.1006/jmre.1997.1161.

[65] M. H. Levitt and O. G. Johannessen. "Signs of Frequencies and Phases in NMR: The Role of Radiofrequency Mixing." *J. Magn. Reson.*, 142(1):190–194 (2000). doi: 10.1006/jmre.1999.1929.

[66] The instrument constructed from these non-specialized test and measurement equipment suffered from two drawbacks: first, a data size limitation, and, second, slow communication between programmed commands and actual execution on the hardware. For a spectrometer constructed from non-specialized components, higher-end test and measurement equipment with a larger storage memory could address the first limitation, as could a standard analog quadrature mixer and filter scheme, both of which were beyond the scope of this study. The second limitation may be overcome with test and measurement instruments providing USB 3.0 capabilities.

[67] O. Neudert, H.-P. Raich, C. Mattea, S. Stapf, and K. Münnemann. "An Alderman–Grant resonator for S-Band Dynamic Nuclear Polarization." *J. Magn. Reson.*, 242:79–85 (2014). doi:10.1016/J.JMR.2014.02.001.

[68] S. Ahola, J. Perlo, F. Casanova, S. Stapf, and B. Blümich. "Multiecho sequence for velocity imaging in inhomogeneous rf fields." *J. Magn. Reson.*, 182(1):143–151 (2006). doi:10.1016/j.jmr.2006.06.017.

[69] Q. Bao, J. Feng, L. Chen, F. Chen, Z. Liu, B. Jiang, and C. Liu. "A robust automatic phase correction method for signal dense spectra." *J. Magn. Reson.*, 234:82–89 (2013). doi:10.1016/j.jmr.2013.06.012.

[70] M. Sawall, E. von Harbou, A. Moog, R. Behrens, H. Schröder, J. Simoneau, E. Steimers, and K. Neymeyr. "Multi-objective optimization for an automated and simultaneous phase and baseline correction of NMR spectral data." *J. Magn. Reson.*, 289:132–141 (2018). doi: 10.1016/j.jmr.2018.02.012.

[71] V. A. Mandelshtam. "FDM: The filter diagonalization method for data processing in NMR experiments." *Prog. Nucl. Magn. Reson. Spectrosc.*, 38(2):159–196 (2001). doi:10.1016/S0079-6565(00)00032-7.

[72] J. C. Hoch. "Beyond Fourier." *J. Magn. Reson.*, 283:117–123 (2017). PMID: 28385517. doi: 10.1016/j.jmr.2017.03.017.

[73] M. A. Zambrello, A. D. Schuyler, M. W. Maciejewski, F. Delaglio, I. Bezsonova, and J. C. Hoch. "Nonuniform sampling in multidimensional NMR for improving spectral sensitivity." *Methods*, 138-139:62–68 (2018). PMID: 29522805. doi:10.1016/j.ymeth.2018.03.001.

[74] S. G. Hyberts, K. Takeuchi, and G. Wagner. "Poisson-gap sampling and forward maximum entropy reconstruction for enhancing the resolution and sensitivity of protein NMR data." *J. Am. Chem. Soc.*, 132(7):2145–2147 (2010). PMID: 20121194. doi:10.1021/ja908004w.

[75] A. S. Stern, K. B. Li, and J. C. Hoch. "Modern spectrum analysis in multidimensional NMR spec-

troscopy: Comparison of linear-prediction extrapolation and maximum-entropy reconstruction." *J. Am. Chem. Soc.*, 124(9):1982–1993 (2002). PMID: 11866612. doi: 10.1021/ja011669o.

[76] M. Levien, M. Reinhard, M. Hiller, I. Tkach, M. Bennati, and T. Orlando. "Spin density localization and accessibility of organic radicals affect liquid-state DNP efficiency." *Phys. Chem. Chem. Phys.*, 23(8):4480–4485 (2021). doi:10.1039/D0CP05796G.

[77] M. Levien, M. Hiller, I. Tkach, M. Bennati, and T. Orlando. "Nitroxide Derivatives for Dynamic Nuclear Polarization in Liquids: The Role of Rotational Diffusion." *The Journal of Physical Chemistry Letters*, 11(5):1629–1635 (2020). doi:10.1021/acs.jpclett.0c00270.

[78] A. Jerschow and N. Müller. "Efficient Simulation of Coherence Transfer Pathway Selection by Phase Cycling and Pulsed Field Gradients in NMR." *J. Magn. Reson.*, 134(1):17–29 (1998). doi:10.1006/jmre.1998.1491.

[79] J. Keeler. *Understanding NMR Spectroscopy*. John Wiley & Sons (2011). ISBN 978-1-119-96493-3. Google-Books-ID: WUmCpq30pygC.

[80] S. Saxena and J. H. Freed. "Absorption lineshapes in two-dimensional electron spin resonance and the effects of slow motions in complex fluids." *J. Magn. Reson.*, 124(2):439–54 (1997). PMID: 9169224. doi: 10.1006/jmre.1996.1078.

[81] B. Dzikovski, V. V. Khramtsov, S. Chandrasekaran, C. Dunnam, M. Shah, and J. H. Freed. "Microsecond Exchange Processes Studied by Two-Dimensional ESR at 95 GHz." *J. Am. Chem. Soc.*, 142(51):21368–21381 (2020). doi:10.1021/jacs.0c09469.